# POLITECNICO DI TORINO

Master Degree in Energy and Nuclear Engineering

Master Degree thesis

# Modelling eddy currents in superconducting magnets for fusion reactors


Supervisor
Prof. Roberto Bonifetto
Dott. Andrea Zappatore

Candidate
Marco De Bastiani

October 2021

# Abstract

The confinement of the plasma in fusion devices is guaranteed by means of suitable magnetic fields that are generated, in the tokamak configuration, by three different set of coils. In the case of the toroidal field (TF) superconducting magnets during operation a steady current is imposed within the coil, generating a mainly toroidal stationary magnetic field. The evaluation of the static magnetic field has been performed here by means of the finite element (FE) open-source code FreeFem++. For the evaluation of static field in relevant cases for fusion applications, a fully 3D tool has been developed; it has been benchmarked both against simple analytical cases (e.g. Biot-Savart law) and against data obtained by means of state of the art software in a real-case application (DTT TF coils).
In presence of multiple coils with huge transport current, strong Lorentz forces arise between different windings and bulky metallic structures are needed to withstand them. Due to the normal pulsed coil operation during the plasma scenario, or due to the fast current discharge or plasma disruption in off-normal operations, the magnetic field varies in time. According to Faraday's law, a time varying magnetic field induces an electric field that directly generates eddy currents in the TF structures. These currents, due to the non-null electrical resistivity of the metal, generate heat in the structure close to the winding pack reducing the temperature margin of the superconducting cables. The Joule power generated is a fundamental input for the thermal-hydraulic (TH) analysis of the magnet. A model for the evaluation of the eddy currents is required; however, this is a challenging topic since a transient, fully 3D electromagnetic (EM) model is needed.
This transient analysis has also been faced here by means of the FE open source code FreeFem++, that is the same adopted by the 4C code for the thermal analysis of the magnet structures. First, the correct implementation of the transient EM model is verified by means of suitable benchmarks

against both classical literature benchmarks and more realistic situations with results obtained with state of the art FE commercial codes. Then the following strategy is pursued: the EM model is used for the evaluation of magnetic field evolution and induced eddy currents in the selected transient. Once the generated eddy current density is known, the deposited Joule power is evaluated by means of the Ohm law. The power deposition is then used as input for the TH analysis carried out with the 4C code with, the objective of evaluating the time evolution of the temperature margin in the superconducting cables. This approach is general and valid for any situation provided that the correct geometry and problem definition is used as input to the tool. This strategy has been applied here to the analysis of the fast current discharge in a TF coil of the DTT. Particular attention is given to the newly developed 3D transient EM model. Also the results of the complete (EM + TH) analysis are presented and discussed in this work.

Alle persone che mi supportano e mi sopportano.

# Contents

# List of Figures

# List of Tables

# List of Symbols

| Symbol | Description | Units |
|---|---|---|
| A | Surface | $[m^2]$ |
| $\overrightarrow{A}$ | Vectorial magnetic potential | [T/m] |
| $\overrightarrow{B}$ | Vectorial magnetic induction | [T] |
| dt | Adopted time step in transient simulation | [s] |
| E | Deposited energy | [J] |
| $\overrightarrow{E}$ | Vectorial electric field | [V/m] |
| $\epsilon_{rel}$ | Relative error between two values | [-] |
| $\varepsilon_0$ | Dielctric vacuum constant | [F/m] |
| $\Gamma$ | Surface border of the 3D domain | $[m^2]$ |
| $h_c$ | Height of the single conductor including the jacket | [mm] |
| I | Integral current | [A] |
| $\overrightarrow{J}$ | Vectorial current density | $[A/m^2]$ |
| lay | number of layers adopted for the 3D extrusion of the WP section | [-] |
| $\mu_0$ | Vacuum magnetic permeability | $[H/m]$ |
| $\mu$ | General magnetic permeability | $[H/m]$ |
| n | number of elements on the shorter side of the WP mesh | [-] |
| $\hat{n}$ | Normal vector to a surface | [-] |
| $N_c$ | Number of conductors in the WP | [-] |
| $\nu$ | $1/\mu$ | [m/H] |
| $\Omega$ | General subdomain | $[m^3]$ |
| $\omega$ | Angular velocity | $[rpm]$ |
| P | Power | [W] |
| $q^{III}$ | Power density | $[W/m^3]$ |
| r | General radial coordinate | [m] |
| $R$ | Radius | [m] |

| | | |
|---|---|---|
| $\sigma$ | Electrical conductivity | [S/m] |
| t | Time | [s] |
| $t_0$ | Time of dump beginning | [s] |
| T | Temperature | [K] |
| $\tau$ | exponential dump time constant | [s] |
| $t_{dpins}$ | Double pancake insulation thickness | [mm] |
| $t_{groundins}$ | Ground insulation thickness | [mm] |
| $t_{turnins}$ | Turn insulation thickness | [mm] |
| V | Volume | $[m^3]$ |
| $w_c$ | Width of the single conductor including the jacket | [mm] |

# Subscripts

| | |
|---|---|
| 0 | Initial value |
| *boundary* | Property evaluated at the boundary of the domain |
| $c$ | Referred to the conductor |
| $CS$ | Current sharing |
| *eddy* | Referred to eddy currents |
| $HS$ | Hot spot |
| $in$ | inlet |
| $j$ | Referred to the jacket |
| $k$ | Known location |
| $n$ | $n^{th}$ subvolume |
| *out* | Outlet |
| *Sphere* | Property related to the external world sphere |
| $WP$ | Referred to the Winding pack |
| $x$ | Referred to coordinate x |
| $y$ | Referred to coordinate y |
| $z$ | Referred to coordinate z |

# Acronyms

| | |
|---|---|
| CICC | Cable In Conduit Conductor |
| CCC | Case Cooling Channels |
| DTT | Divertor Tokamak Test |
| EM | Electro Magnetic |
| FE | Finite Element |
| FEM | Finite Element Method |
| FF++ | FreeFem++ |
| PF | Poloidal Field |
| SC | Super Conducting |
| TF | Toroidal Field |
| TH | Thermal-Hydraulics |
| WP | Winding Pack |

# Introduction

## Framework

Today, as never before, the decarbonisation is a central topic in political and economical discussions. In this framework the role of energy production is central, given that it is the major responsible of greenhouse gases production. Regardless the political choices of the different countries, the innovation in energy production is fundamental for the substitution of fossil fuels as energy source. New solutions must be adopted using both renewables and nuclear power.
In the field of nuclear power the fusion is considered to have an important role in the future of energy production since it is considered to be a potentially unlimited and almost clean energy source based on the Deuterium - Tritium nuclear fusion reaction.
To most promising way to produce fusion reactions on earth is by means of magnetic confinement of the plasma, in which the Deuterium and Tritium ions find the conditions favorable to fusion. Given that the plasma particles are fully ionized the presence of a properly shaped magnetic field assure their confinement. The required magnetic fields are extremely high and for their production superconducting (SC) magnets are adopted in all the facilities nowadays in construction or design phase. SC magnets are adopted since, under certain conditions, they offer no resistance to the flowing of the current and so it is possible to increase the current magnitude, increasing so the generated magnetic field, without the risk of having excessive power deposition in the coils. By the way nuclear fusion is not a mature technology yet and a lot of research is required to reach the final objective of producing the first kWh of electricity to be introduced in the grid. The pathway to reach this goal is, however, very well studied and detailed in the roadmap towards fusion energy [1] [27].

The milestones of this roadmap are directly correlated to the development of two key projects. The first one is ITER. Originally ITER standed to International Thermonuclear Experimental Reactor, but today the latin meaning (the way) is considered. This machine is currently going to be built in Cadarache (France) with the aim of proving the possibility of exploiting nuclear fusion as a large-scale and carbon-neutral energy source. ITER is expected to be the first fusion machine able to have a net power production sustaining the fusion reaction for long periods.
The second project is the EU DEMO reactor, the successor of ITER, that has just started (2021) its conceptual design phase and that is expected to be the first fusion machine able to produce electricity to be sent to the grid within the 50s of this century, demonstrating the economical feasibility of the technology.
The European roadmap just described is summarized in figure 1.

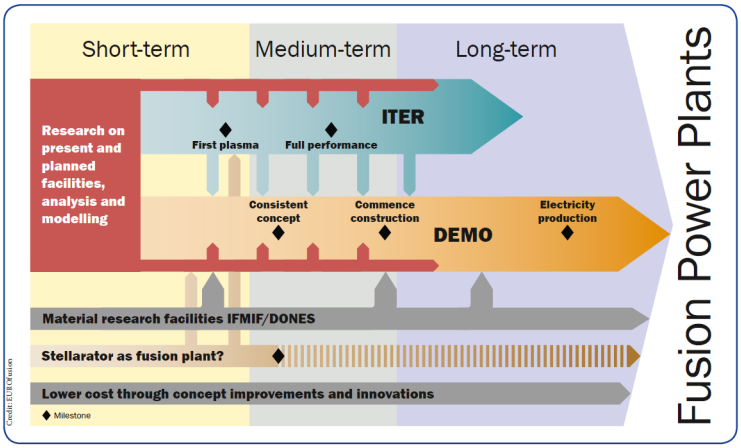


Figure 1: Summary of the European Roadmap to fusion energy. Reproduced from [27]

Moreover, together with the above mentioned machines, several side projects are currently ongoing with fundamental impact on the technology development such as the Divertor Tokamak Test (DTT) facility that is expected to contribute to the solution of the power exhaust issue in the EU DEMO and that will be built at the ENEA laboratories in Frascati (Italy) in the next few years.
Together with the experimental analyses that are foreseen in the next years

a strong effort is required also from the computational point of view, with the aim of supporting the design, the performance optimization and the operation of the devices, including the extremely multi-physical nature of the problem. This thesis work is inserted in this numerical simulation framework and in the DTT context too.

## Aim and structure of the work

This thesis work aims to develop a tool capable of evaluating the power deposition in the bulky structures of superconducting magnets for fusion reactors generated by eddy currents during transients, in turn due to magnetic field variations. The evaluation of this power is of fundamental importance to perform a detailed thermal - hydraulic transient simulation since it is part of the heat load to be considered acting on the SC cables and cooperating in the erosion of the temperature margin.
The aim is to develop the tool in the most flexible way, so that any geometry and configuration can be properly treated, and with the idea of making it fully compatible with the 4C code [13], the state of the art tool for thermal - hydralic simulation of magnets for fusion reactors, developed at Politecnico di Torino, that is used to evaluate the temperature margin evolution during the transient. In order to develop the tool by means of an open source software, FreeFem++ for the FE(finite element) solution of the problem and GMSH for the mesh generation. The advantage of this choice is that with GMSH mesher any kind of geometry can be meshed and then imported in FreeFem++ is used for the problem solution. Moreover the chosen FE tool is the same adopted for the thermal computation included in the 4C code, ensuring its compatibility with the thermal - hydraulic module.
Before the development of the actual electrodynamic model for eddy currents evaluation, a magnetostatic analysis is carried out developing a tool able to evaluate the steady state magnetic field generated during steady-state operation. The DTT TF has been chosen as a test case. The main aim of this part, included in chapter one, is to start learning the physics and checking the capability of the software to properly solve the problem, both in self - field and tokamak configuration. The results have been verified performing a benchmark against those obtained with the commercial code OPERA [28] in ENEA.

In the second chapter the description of the electrodynamic model adopted in the tool used for eddy current evaluation is described both from a theoretical point of view, and from the numerical point of view, with its FreeFem++ structure. Before using the tool in real relevant cases it has been verified in simple problems to assess its reliability. The first problem in which it has been used is a classical literature benchmark: the Felix brick (TEAM 4 problem) [9]. This problem is the very first step since the driver, the time varying magnetic field, is prescribed and so the tool is not required to evaluate it (e.g. with a magnetostatic analysis as that mentioned above). By the way in the real case application the tool must be able to self compute the evolution of the magnetic field and, for this reason, a simplified coil model is developed and the verification is performed comparing the results with those coming from the commercial FE software COMSOL [29].
Given the extraordinary complexity of the problem from the numerical point of view, generating extremely massive meshes, the parallel computing is considered to be an important strategy to reduce the computational time. In chapter two a brief introduction to parallel computing and its possible application is included too.
The third chapter is dedicated to the description of the application of the developed tool in a real case situation that is the fast current discharge in the DTT TF coil. A detailed description of the set up of the simulation and the grid independence analysis are provided together with the final results concerning the power deposition in the coil structures.
This last result is the connection between the electrodynamic and the thermal - hydraulic parts since it used as a driver in the thermal-hydraulic analyses. In chapter four, after a brief introduction to the 4C code, the coupling strategy between the two separate tools is described and then the results concerning the temperature evolution in the different coil components are presented and discussed with particular focus on the evolution of the temperature margin in the coil strands. This closes the work since an integrated multi physical tool capable of obtaining information coming from the electrodynamic model as input for the thermal - hydraulic one is fully developed and applicable, in general, to all the possible geometries and configurations.
As a conclusion, the possible future development and improvement are pointed out, including the addition to the tool of the thermo-mechanical part, but also the validation of the existing tool thanks to the comparison with the results of future experimental campaigns (e.g. DTT cold test facility) and the improvement of the coupling strategies and of the tool flexibility.

# Chapter 1

# DTT-TF magnetostatic analysis

The current that is flowing in normal operation in the magnets of a fusion machine is responsible of the production of huge magnetic fields that are used to counterbalance the plasma pressure keeping it confined within the plasma chamber. During the plasma pulsed operation the current in the TF coils is constant and a static magnetic field is generated. It is worthwhile to develope an open source tool capable of solving the static equation with also the aim of investigating the physics to be analyzed. The tool has been developed and benchmarked against a simple analytical situation (Biot - Savart law [30]) and then a real case application has been proposed.
As first real case application the magnetostatic analysis of the Toroidal field (TF) coils of DTT has been performed in order to carefully evaluate the magnetic field that is generated by this coil during steady-state operation, benchmarking the results with the outcome obtained in ENEA by means of the OPERA tool [28].
The adopted software is the open source finete element (FE) code FreeFem++ [5] that has been chosen for its high flexibility and the easy way in which it can be coupled with other modules in the perspective of the development of the transient tool to be coupled with the thermal - hydraulic one.

## 1.1 Ampère law and its weak formulation

The physical problem that must be described is the generation of a magnetic field due to the presence of a transport current within a conductor. The

physics of the problem is described by means of the Ampère law (equation 1.1).

$$\nabla \times \overrightarrow{B} = \mu_0(\overrightarrow{J} + \varepsilon_0 \frac{\partial \overrightarrow{E}}{\partial t}) \tag{1.1}$$

Since this first analysis is focused on the magnetostatic behavior of the system the equation 1.1 can be rewritten as:

$$\nabla \times \overrightarrow{B} = \mu_0 \overrightarrow{J} \tag{1.2}$$

Very often this equation can be expressed not directly as a function of the magnetic induction $\overrightarrow{B}$, but as a function of the magnetic vector potential $\overrightarrow{A}$ which is defined as:

$$\overrightarrow{B} = \nabla \times \overrightarrow{A} \tag{1.3}$$

obtainig a new definition of the Ampère Law (equation 1.2) written as follows:

$$\nabla \times (\nabla \times \overrightarrow{A}) = \mu_0 \overrightarrow{J} \tag{1.4}$$

This equation cannot be solved analytically except that in some simple and ideal cases (e.g. Biot Savart problem [30]) and so must be faced numerically. As already mentioned, the numerical method that has been adopted for the solution of the problem is the finite element that are is directly facing the differential equation to be solved, but its weak or variational formulation. To obtain this formulation the strong form must be multiplied by a suitable test function and then integrated on the domain. Making use of the procedure of integration by parts applicable to 3D integrals the formulation can be simplified. Using general notation the Ampère law has the following shape, where $\overrightarrow{u}$ and $\overrightarrow{f}$ are two generic vectorial fields:

$$\nabla \times (\nabla \times \overrightarrow{u}) = \overrightarrow{f} \tag{1.5}$$

Multiplying the equation 1.5 by a suitable test function and integrating over the domain, the first step to obtain the weak formulation of the Ampère law is evaluated.

$$\int_\Omega (\overrightarrow{v} \cdot (\nabla \times (\nabla \times \overrightarrow{u})))d\Omega = \int_\Omega (\overrightarrow{v} \cdot \overrightarrow{f})d\Omega \tag{1.6}$$

A way to integrate this complex structure must be found out to simplify the expression. It is known that the integral of the scalar product of the curl of a vector and another vector is given as:

$$\int_{\Omega}(\nabla \times \overrightarrow{u}) \cdot \overrightarrow{v}\, d\Omega = \int_{\Omega} \overrightarrow{u} \cdot (\nabla \times \overrightarrow{v}) d\Omega - \int_{\partial\Omega} (\overrightarrow{u} \times \hat{n}) \cdot \overrightarrow{v}\, dS \qquad (1.7)$$

The correlation provided by equation 1.7 can be used to integrate the first term of the equation 1.6 remembering that the curl of a vector is a vector itself.

$$\int_{\Omega} \nabla \times \underbrace{(\nabla \times \overrightarrow{u})}_{\overrightarrow{g}} \cdot \overrightarrow{v} = \int_{\Omega} \overrightarrow{g} \cdot (\nabla \times \overrightarrow{v}) d\Omega - \int_{\partial\Omega} (\overrightarrow{g} \times \hat{n}) \cdot \overrightarrow{v}\, dS \qquad (1.8)$$

Substituting the corresponding value of $\overrightarrow{g}$ in equation 1.8 and introducing the obtained result in equation 1.6 it is possible to obtain the simplified version of the weak formulation of the Ampère law.

$$\int_{\Omega}(\nabla \times \overrightarrow{u}) \cdot (\nabla \times \overrightarrow{v}) d\Omega = \int_{\Omega} \overrightarrow{f} \cdot \overrightarrow{v}\, d\Omega + \int_{\partial\Omega} ((\nabla \times \overrightarrow{u}) \times \hat{n}) \cdot \overrightarrow{v}\, dS \quad (1.9)$$

For boundary conditions reasons the last term of equation 1.9 can be simplified since $\overrightarrow{u} \times \hat{n} = 0$, thus obtaining the final simplified version of the Ampère law weak formulation:

$$\int_{\Omega}(\nabla \times \overrightarrow{u}) \cdot (\nabla \times \overrightarrow{v}) d\Omega = \int_{\Omega} \overrightarrow{f} \cdot \overrightarrow{v}\, d\Omega \qquad (1.10)$$

Now, substituting to the general expression $\overrightarrow{u}$ and $\overrightarrow{f}$ the real quantities that are describing the magnetostatic phenomena, the definitive weak formulation that will be faced by means of FEM is obtained.

$$\int_{\Omega} \frac{1}{\mu}(\nabla \times \overrightarrow{A}) \cdot (\nabla \times \overrightarrow{v}) d\Omega - \int_{\Omega} \overrightarrow{J} \cdot \overrightarrow{v}\, d\Omega = 0 \qquad (1.11)$$

The solution of the steady state problem is performed by using nodal finite elements, that are requiring few memory with respect to the edge ones, but, in order to ensure the Coulomb gauge condition, an additional term must be added as reported in equation 1.12 assuring that the field is divergence free.

$$\int_{\Omega} \frac{1}{\mu}(\nabla \times \overrightarrow{A}) \cdot (\nabla \times \overrightarrow{v}) + \frac{1}{\mu}(\nabla \cdot \overrightarrow{A}) \cdot (\nabla \cdot \overrightarrow{v}) d\Omega - \int_{\Omega} \overrightarrow{J} \cdot \overrightarrow{v}\, d\Omega = 0 \quad (1.12)$$

## 1.2 Benchmarking against analytical solution - Biot-Savart law

Before applying the magnetostatic tool to the foreseen real case, it has been applied, for benchmarking purposes, to a very simple case, to be compared with the Biot-Savart analytical solution. The Biot-Savart law is strictly true for the evaluation of the magnetic field generated by an infinite cable carrying a current, and is obtained by integration of the Ampère law. Clearly it is not possible to model an infinite cable, but having a ratio between the cable length and the cable diameter sufficiently big, the Biot-Savart law can be assumed to be valid also for a non infinite cable.
The proposed geometry is a cable of 1 $[m]$ length with the diameter of 1 $[cm]$. This configuration provides a length to diameter ratio of 100, considered to be large enough to apply the Biot-Savart law outside the conductor. For simulation purposes the external world must be modeled too, and in this case a 2 $[m]$ radius sphere has been adopted. A representation of the geometry is shown in figure 1.1.

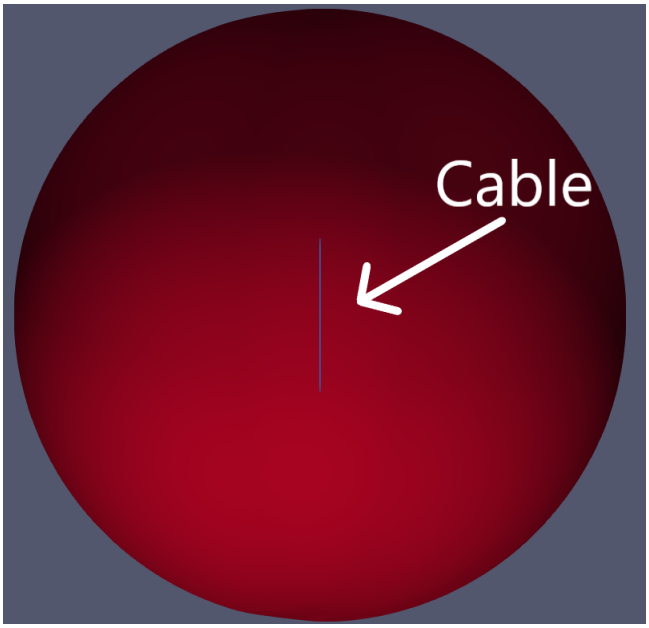


Figure 1.1: Domain of the simulation to be benchmarked against the Biot-Savart law.

In this picture the cable is highlighted in blue and in it a steady current of $1000\,[A]$ flowing upward has been imposed. The magnetic permeability has been assumed to be uniform and equal to the vacuum one ($\mu = 4\pi \cdot 10^{-7}\,[H/m]$).
According to Biot-Savart law the magnetic field all around the cable can be evaluated as reported in equation 1.13.

$$|\overrightarrow{B}(r)| = \mu \cdot \frac{I}{2\pi r} \tag{1.13}$$

In figure 1.2 the comparison between the analytical result and the FEM result obtained with the above described model is shown.

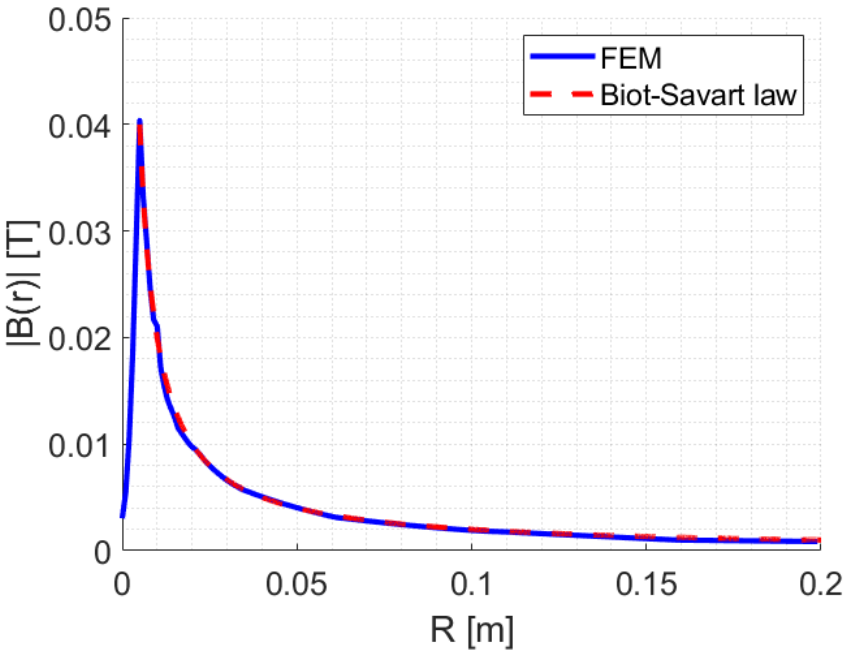


Figure 1.2: Comparison between analytical and numerical results. Biot-Savart law.

The finite element results are absolutely comparable with the analytical solution proposed by Biot-Savart outside the conductor since the behavior inside the conductor can't be described by this law that is assuming the cable to be 1D in the axial direction, concentrating the current basically in the

center of the real conductor.
It must be pointed out that the Biot-Savart problem could be better reproduced in a 2D configuration solving the problem in a plane perpendicular to the cable, but here, for benchmarking purposes of the 3D tool, this configuration has been chosen.

## 1.3 DTT TF - Geometry and Materials

The magnet system that will be used to confine the plasma in DTT is composed of coils obtained by windings of superconducting Cable-In-Conduit-Conductors (CICCs) cooled by supercritical Helium entering at almost 4.5 [K] and almost 5 [bar] [2]. What is relevant for the present work is the geometry and structure of the Toroidal Field Coils. They are 18 separated coils that are disposed in a toroidal geometry forming the envelope of the plasma chamber (figure 1.3).

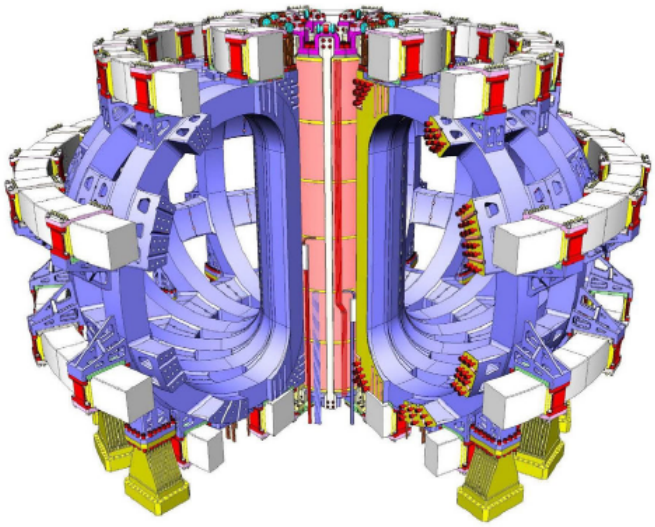

Figure 1.3: View of the entire magnet system. Reproduced from [2]

The shape of the Toroidal Field Coil is symmetric with respect to the equatorial plane following a "D-shape" and the winding pack has the section

as reported in figure 1.4.

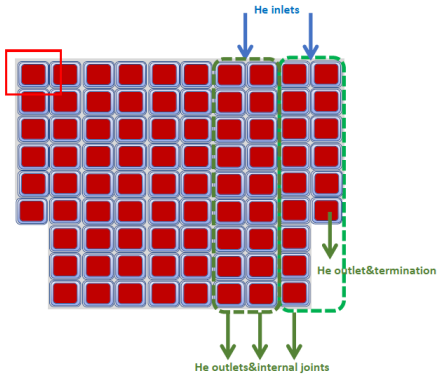


Figure 1.4: Section of the DTT TF coil winding pack. Reproduced from [22].

Some geometrical data referring to the coil section dimensions are reported in the following table (Table 1.1).

Table 1.1: Geometrical data of the winding pack [22].

| **Quantity** | **Description** | **Value [mm]** |
|---|---|---|
| $w_c$ | Width of the single conductor including the jacket | 28.8 |
| $h_c$ | Height of the single conductor including the jacket | 22.1 |
| $t_{turnins}$ | Turn insulation thickness | 1.0 |
| $t_{dpins}$ | Double pancake insulation thickness | 0.5 |
| $t_{groundins}$ | Ground insulation thickness | 2.0 |

For the sake of simulating the magnetostatic behavior of the TF Coil only the part containing the conductors has been modeled generating a fully 3D geometry representing the coil itself. The geometry has been completely developed parametrically in the FreeFem++ environment. The coil geometry that has been produced is shown in figure 1.5.
For the sake of performing the magnetostatic analysis, the section of the coil has been homogenized defining the current, properly scaled on the conductor surface, on the entire section. This assumption is neglecting the presence of jacket and insulation; this is considered to be a valid assumption for magnetostatic analysis. The rationale behind it is that macroscopically the field is

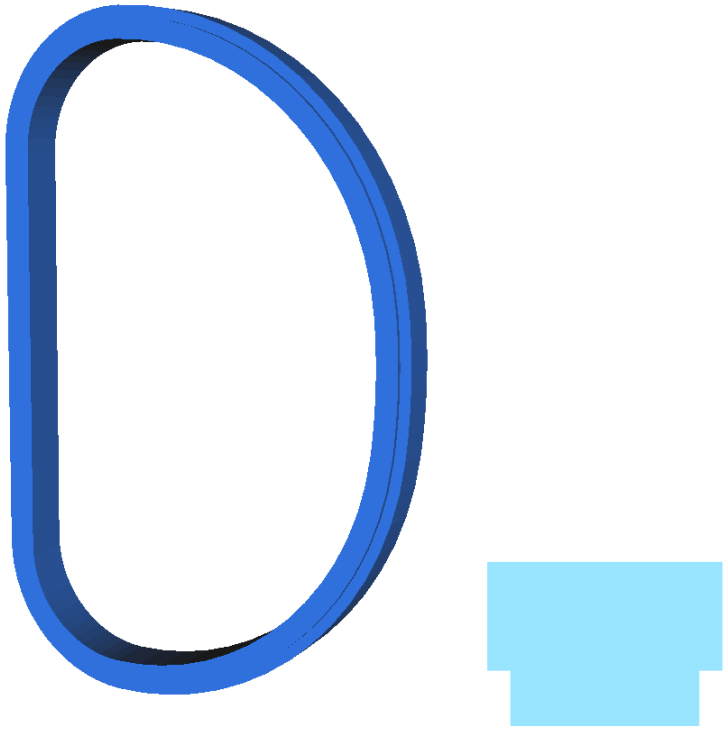

(a) (b)

Figure 1.5: Geometrical model of the DTT TF: full 3D model (a) and its equatorial section (b)

supposed not to be affected by where the current is actually defined, but is only relevant that integrally the current is properly defined; this assumption is loosing some level of detail from the conductor level point of view, where the presence of insulation material perturbs locally the field. In any case this perturbation is considered not to be relevant for the purposes of this work, mainly dealing with the analysis of the behavior within the casing, outside the winding pack.
The material properties are considered not to be relevant in the magnetostaitc analysis, indeed the structures are not included in this computation and neither the insulate materials, and so the only material that would be modeled is the $Nb_3Sn$ in the SC cables. By the way the only property that is relevant for the solution of the described problem is the magnetic permeability ($\mu$) of

the conductor that is assumed to be equal to the vacuum magnetic permeability, and the same is true for the external air too. So that $\mu = 4\pi \cdot 10^{-7}[H/m]$.

## 1.4 DTT TF - Simulation Setup

The geometry that has been proposed in the previous section is not sufficient to simulate the magnetostatic behavior of the coil since, as it is possible to demonstrate, the flux of magnetic field across any surface is null. This means that the magnetic field is solenoidal and all the field lines are closed. This in principle would require an infinite computational domain to close all the field lines. Clearly this is impossible and in order to model as precisely as possible the magnetostatic behavior a sufficiently big external environment has been introduced. This external environment has been modeled as a sphere with radius $R_{sphere} = 10[m]$. The overall computational domain is shown in Figure 1.6.

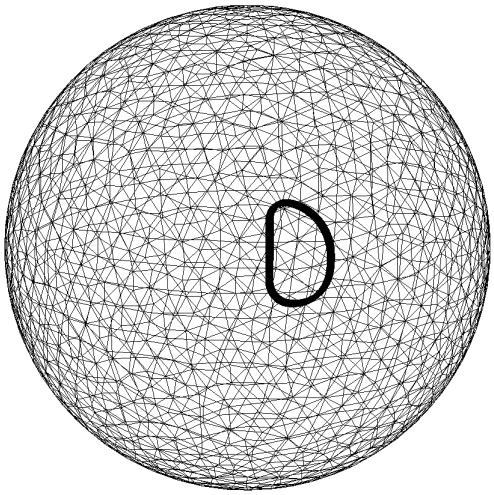

Figure 1.6: Computational domain of the DTT TF magnetostatic analysis

Even if the external environment that has been introduced is not strictly the real environment, since it is not infinite, a suitable boundary condition must be fixed in order to close the problem. Since moving far away from

the field source the potential is expected to decrease, at the sphere walls the magnetic vector potential has been fixed to be equal to zero.

$$\overrightarrow{A}_{Boundary} = 0 \tag{1.14}$$

Given that the problem is, by the time, steady state, no initial conditions are required.
As already mentioned, the numerical model that has been adopted for the solution of the problem is the finite element. By means of the FEM the differential problem is translated in a big algebraic system of equations that can be solved both with a direct solver or with an iterative scheme. Given that the size of the computational domain is big such as the amount of cells involved in the discretization of the space, in this case an iterative solver has been considered to be more feasible and the conjugate gradient (CG) method, already implemented in FreeFem++, has been adopted. As all the algebraic systems of equations also the resulting system of the FEM version of the Ampère law can be expressed in matricial form as follow:

$$[A] \cdot \overrightarrow{x} = \overrightarrow{b} \tag{1.15}$$

Using an iterative method implies the production of a sequence of vectors $\{\overrightarrow{x}^k, k > 0\}$ that converges to the exact solution [3]. In general any iterative procedure can be expressed as follows:

$$[P] \cdot (\overrightarrow{x}^{(k+1)} - \overrightarrow{x}^{(k)}) = \alpha_k \cdot \overrightarrow{r}^{(k)} \tag{1.16}$$

where $\overrightarrow{r}^{(k)}$ is the residual at the iteration k evaluated as $\overrightarrow{r}^{(k)} = \overrightarrow{b} - [A] \cdot \overrightarrow{x}^{(k)}$ and $\alpha_k \neq 0$.
The conjugate gradient method is a dynamic method in which $\alpha_k$ is not constant and changes during the iterations, assuring the minimization of the error along the descent direction $\overrightarrow{p}^{(k)}$. The conjugate gradient method can be summarized with the following algorithm for $k = 0, 1, ...$

$$\alpha_k = \frac{\overrightarrow{p}^{(k)T} \cdot \overrightarrow{r}^{(k)}}{\overrightarrow{p}^{(k)T}[A]\overrightarrow{p}^{(k)}} \tag{1.17}$$

$$\overrightarrow{x}^{(k+1)} = \overrightarrow{x}^{(k)} + \alpha_k \overrightarrow{p}^{(k)} \tag{1.18}$$

$$\overrightarrow{r}^{(k+1)} = \overrightarrow{r}^{(k)} - \alpha_k[A] \cdot \overrightarrow{p}^{(k)} \tag{1.19}$$

$$\beta_k = \frac{([A] \cdot \overrightarrow{p}^{(k)})^T \cdot \overrightarrow{r}^{(k+1)}}{([A] \cdot \overrightarrow{p}^{(k)})^T \cdot \overrightarrow{p}^{(k)}} \tag{1.20}$$

$$\overrightarrow{p}^{(k+1)} = \overrightarrow{r}^{(k+1)} - \beta_k \overrightarrow{p}^{(k)} \tag{1.21}$$

$$\tag{1.22}$$

## 1.5 Mesh Generation

The mesh of the overall computational domain has been produced in different steps. First of all the 2D mesh of the section has been generated. FreeFEM++ allows to triangulate a surface knowing the borders that are closing it, that are defined in a parametric way. For each border the number of vertexes lying on it can be imposed; in this case the number of vertexes for each border has been fixed in such a way to obtain a mesh as uniform as possible in all the different mesh refinements that have been proposed (i.e the number of vertexes lying on the border is proportional to its length). In Figure 1.7 a mesh example for the 2D section is shown.

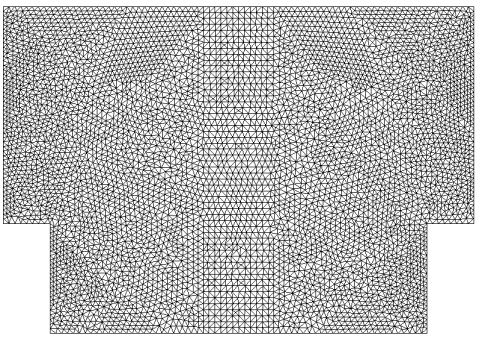

Figure 1.7: Mesh of the 2D section of the WP

This 2D mesh has been used as the basis for the production of the 3D

one. As the generatrix is given piece-wise for four different segments of the "above-equatorial" part, also the mesh has been generated producing separately the eight segments that form the overall coil, such that a different region has been produced for each segment, helping in the subsequent definition of the current that is flowing in the coil itself. After generating all the segments, they are glued together to form the overall 3D mesh of the coil. However, in order to match it with the mesh of the external environment, it is necessary to set up also a surface mesh, obtained by a pre-existing command in FreeFem++. In Figure 1.8 an example of the 3D coil mesh is shown.

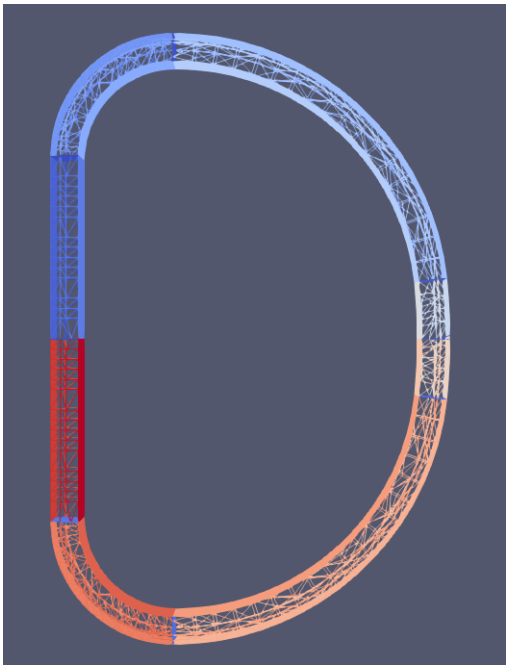

Figure 1.8: 3D mesh of the entire coil. Each color is representative of one of the generatrix segment.

The external environment has been meshed by means of a pre-existing command in FreeFem++ able to mesh the surface of a sphere that has been used, as already mentioned in the previous section, as representative of the environment surrounding the coil. Then the two surface meshes have been glued and finally converted in a volume mesh by means of the external library TetGen that is a tetrahedral mesh generator that creates 3D triangulations

of polyhedral domains using Delaunay-based algorithms [4]. The final result is shown in Figure 1.9.

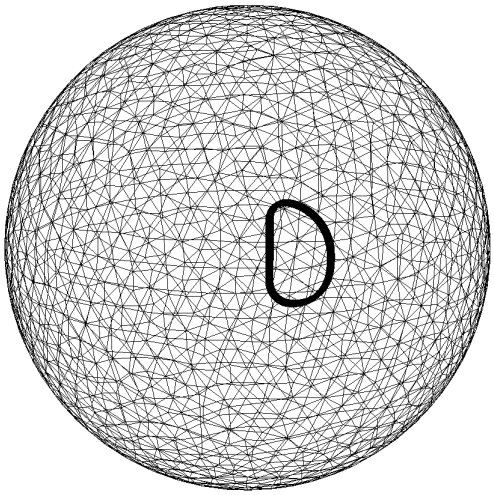

Figure 1.9: View of the overall mesh.

In order to perform the mesh refinement and perform the grid independence of the solution, two parameters have been mainly used: the parameter $n$ and the parameter *lay* that are respectively the number of vertexes on the shorter border of the 2D section and the number of layers in which the 3D extrusion has been discretized. The mesh refinement has been carried out varying both the parameters.
The grid independence analysis has been performed looking at the value of the magnetic field in the center of the first turn of the first pancake in the equatorial inboard plane this location is identified by the coordinates $x_k = -140.60[mm]; y_k = 1135.45[mm]; z_k = 0.0[mm]$ with the origin of the axes fixed at the torus center. In Table 1.2 a summary of the different mesh refinements that have been adopted is reported.

Table 1.2: Adopted meshes for Grid Independence Analysis.

| **Mesh identifier** | **Number of cells** | $n$ | $lay$ | $\mathbf{B}(x_k, y_k, 0.0)$ |
|---|---|---|---|---|
| 1 | 405008 | 6 | 10 | 4.85834 [T] |
| 2 | 805133 | 8 | 15 | 4.83844 [T] |
| 3 | 1088164 | 10 | 15 | 4.83477 [T] |
| 4 | 1341931 | 10 | 20 | 4.83505 [T] |
| 5 fine | 1828874 | 12 | 22 | 4.83309 [T] |
| 6 | 2101397 | 13 | 23 | 4.83384 [T] |

The obtained results for the Grid Independence are also shown graphically in the plot in Figure 1.10.

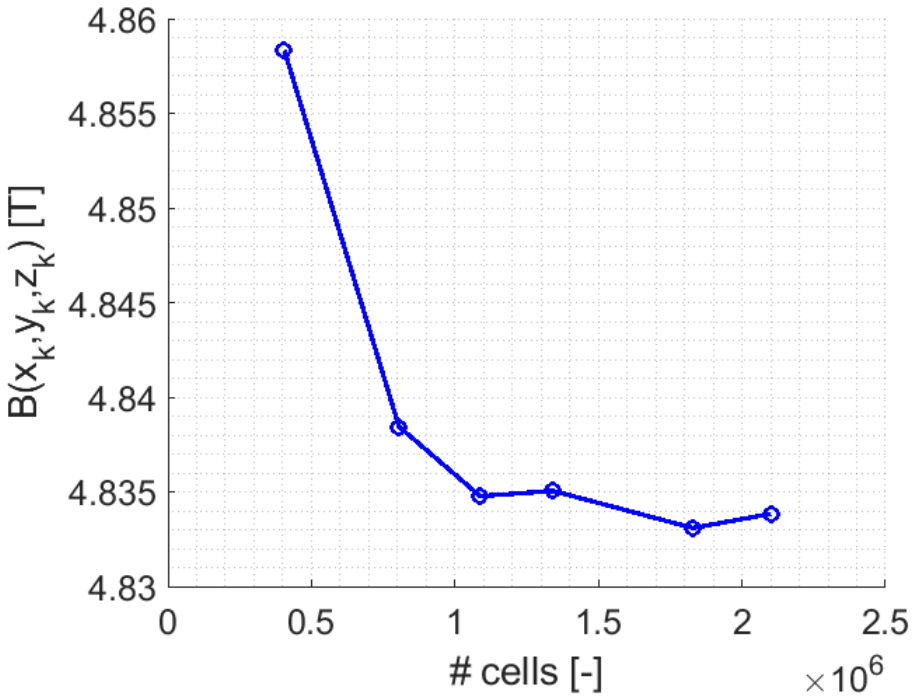


Figure 1.10: Grid Independence Analysis.

It is possible to state that the grid independence of the results is reached since the relative difference between the results obtained with the meshs 5

and 6 is of the order of 0.015%. In order to reduce the computational cost, given the reached grid independence, the mesh number 4 has been adopted for the computations.

## 1.6 Results. Computed magnetic field and benchmarking

The results have been collected and presented here divided into two sections, the first one dedicated to the outcomes obtained in the so called self field configuration, that is the case in which a single TF is operated, the second one including all the 18 TF coils operated together in the tokamak configuration. Both the configurations are relevant since the first one is representative of the situation that will be tested in the cold test facility, while the second one represent the entire machine configuration.

### 1.6.1 Self field

The direct outcomes of the simulation as it has been presented in previous sections are the components of the magnetic vector potential $\overrightarrow{A}$. The relevant outcome, however, is the value of magnetic induction generated in each point of the domain. With the magnetic vector potential definition given by Equation 1.3 the components of the magnetic induction are easily evaluated, and then the module of the magnetic induction is computed as follows:

$$|\overrightarrow{B}| = \sqrt{B_x^2 + B_y^2 + B_z^2} \tag{1.23}$$

This allows to produce some maps that are representing the value of the magnetic induction in the space. Figure 1.11 represents the magnetic induction on the equatorial cross section of the coil at inboard and outboard locations.

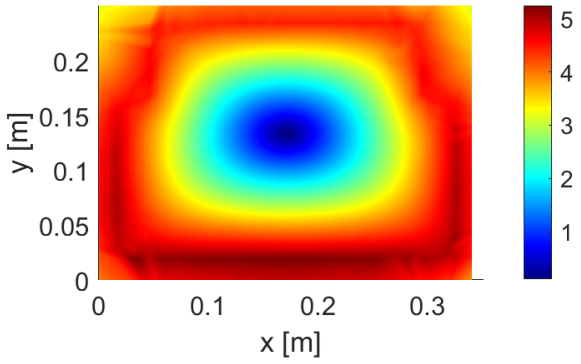


(a)

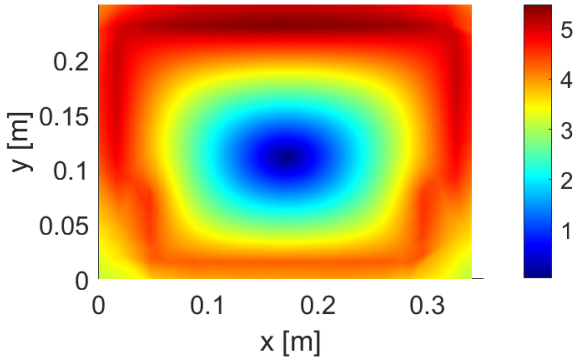


(b)

Figure 1.11: Magnetic induction on equatorial planes at coil inboard (a) and outboard(b) respectively. The coordinate present on the axes are not representative of the position of the coil with respect to the origin, but simply indicate the dimension of the section.

The behavior recalls, macroscopically, the one that can be observed in

the case of any kind of conductor in which current is flowing, in which the magnetic induction rises from the center of the conductor itself up to the borders. Clearly this is not a stand alone conductor, but is a sort of spire and so the inner part of the spire itself is subjected to higher induction as it is possible to see from the darker region on one side of the coil due to the effect caused by the presence of the opposite section of the spire.
The same equatorial plane can be furthermore investigated looking at a bigger section that includes both the inboard and outboard legs of the coil; this view is shown in Figure 1.12, while in Figure 1.13 a 1D plot of the magnetic induction radial profile is shown on the equatorial plane and at $x = 0$.

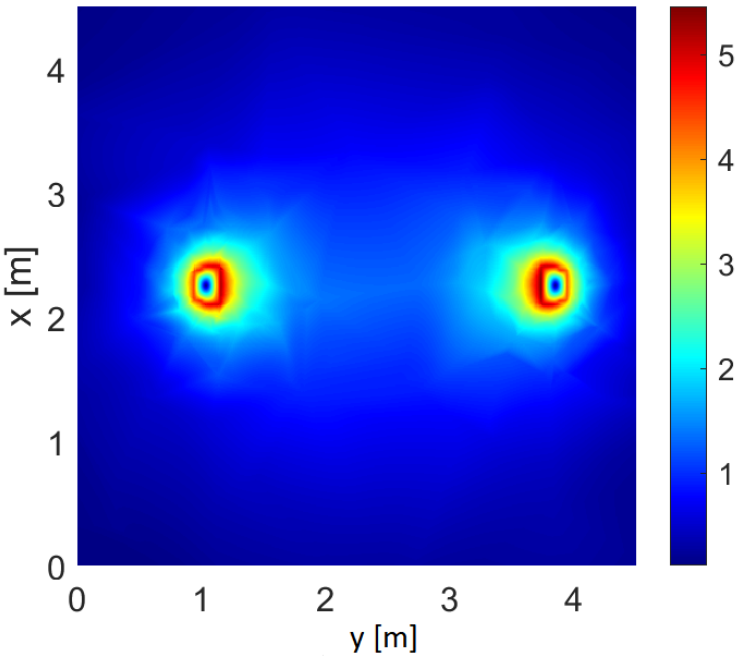


Figure 1.12: Magnetic induction on the equatorial plane. The coordinate present on the axes are not representative of the position of the coil with respect to the origin, but simply indicate the dimension of the section.

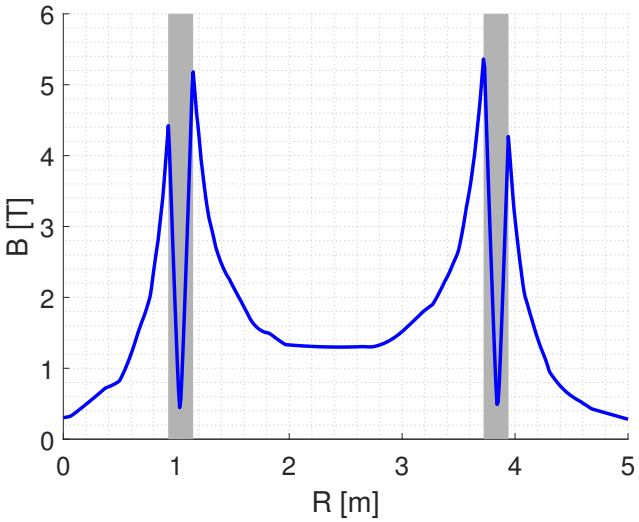


Figure 1.13: Magnetic induction profile in radial direction with respect to the tokamak reference system. In grey highlighted the coordinates at which the WP is located.

From this last picture is even simpler to observe the fact that the maximum induction is reached in the inner part of the coil (the one closer to the plasma) and it is possible to see also the decrease from the outer part of the coil towards the external environment, similar to what happens in case of a single conductor (e.g. Biot-Savart problem). The same observation can be done looking at figure 1.14, in which a radial-vertical section of the coil is shown highlighting the higher induction in the inner part of the coil. Then, within the spire, the magnetic induction is, as expected in presence of a closed electrical loop, almost constant.

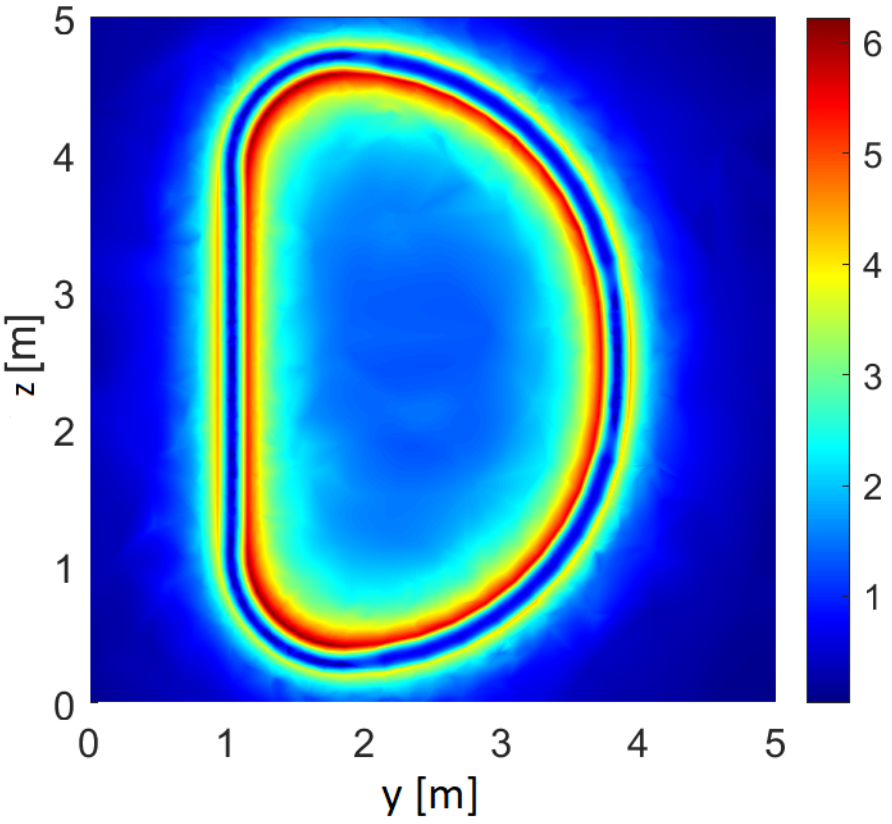


Figure 1.14: Magnetic induction on a coil radial-vertical section. The coordinate present on the axes are not representative of the position of the coil with respect to the origin, but simply indicate the dimension of the section.

### 1.6.2 Tokamak-configuration field

The results that have been described up to now are representative of the so called "self-field" and so the magnetic induction that is generated by the single TF-coil, relevant for the simulation of the experiments that will be performed in the cold test facility. However, as it possible to see from Figure 1.3, the Divertor Tokamak Test facility is composed of 18 TF coils evenly distributed in a toroidal geometry. The distribution of the coils over this toroidal configuration is completely described by the coordinate of the 1x1

conductor (first turn of the first pancake) reported in the following Table (1.3).

Table 1.3: Position of the center of the 1x1 conductor with respect to the machine magnetic axis

| **Quantity** | **Description** | **Value** | **Unit** |
|---|---|---|---|
| $x_{1\times1}$ | X-coordinate of the 1x1 conductor | -140.60 | [mm] |
| $y_{1\times1}$ | Y-coordinate of the 1x1 conductor | 1135.45 | [mm] |

The simulation of the entire set of 18 coils together would require a huge computational power due to the impressive number of cells that would be required for the entire geometry. For this reason the magnetic induction that is generated by the entire set of coils is extracted exploiting the symmetry of the machine itself. Due to the toroidal geometry the model of the entire machine can be limited to the model of only one of the eighteen sectors that are composing the overall 360° geometry, simply imposing cyclic symmetric boundary conditions on the two symmetry planes as discussed also by D'Amico et. al [6]. In order to do that, a modified computational domain has been adopted with respect to the one that has been presented previously. The new computational domain is shown in Figure 1.15.

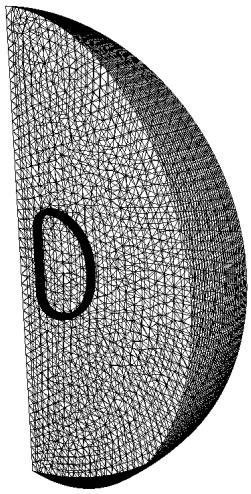

Figure 1.15: Symmetric computational domain

The boundary condition representing the symmetry is basically an homogeneous Neumann that imposes the symmetry of the magnetic induction on the two planes delimiting the spherical sector. The problem is solved, however, as function of the magnetic vector potential and the boundary condition must be translated into a suitable way. In general a boundary condition that represents a plane across which symmetry is verified can be expressed as follows:

$$\overrightarrow{B} \times \hat{n} = 0 \tag{1.24}$$

meaning that no tangential component of the field are expected to exist on that plane. Introducing the potential definition 1.3 this expression becomes:

$$(\nabla \times \overrightarrow{A}) \times \hat{n} = 0 \tag{1.25}$$

This expression can be furthermore simplified introducing the concept of Coulomb gauge according to which the divergence of the magnetic vector potential is null obtaining the following expression [7]:

$$\overrightarrow{A} \cdot \hat{n} = 0 \tag{1.26}$$

With these settings the simulation provides the results representative of the entire machine field generated by the toroidal field coils. The results are here

visualized with the magnetic field map on the TF radial-vertical section in which the difference with respect to the stand alone case is evident: the magnetic induction is much more intense at the inboard part of the coil where the influence of the other coils (which at the inboard are closer to each other than at the outboard) is more relevant. The comparison is clear looking at figure 1.14 and figure 1.16.

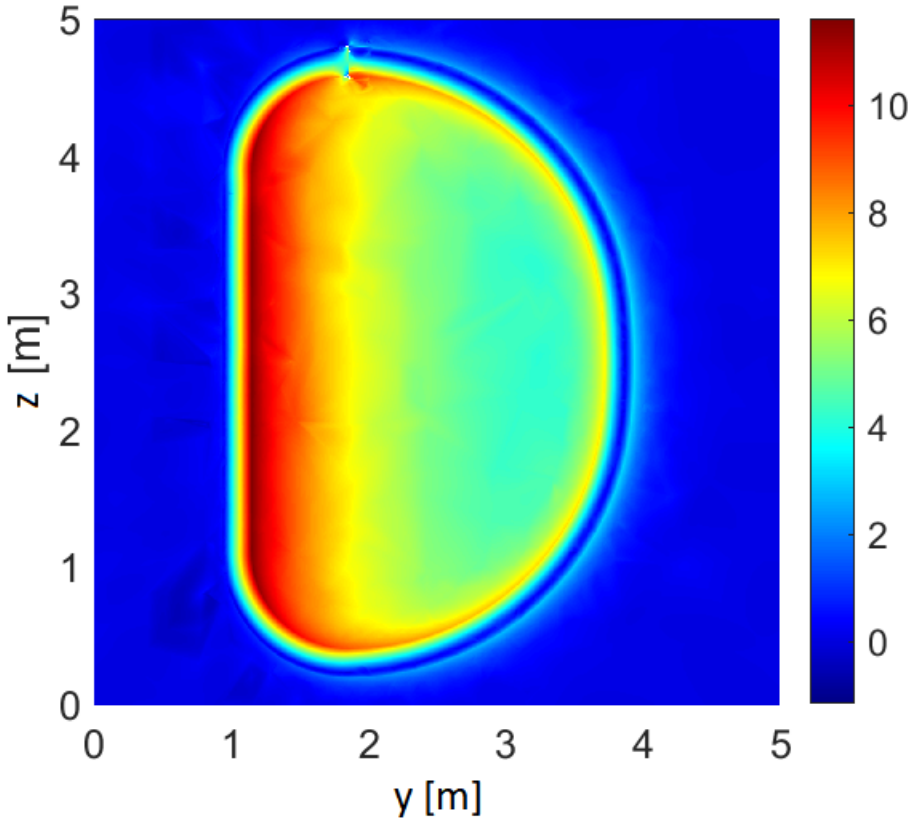


Figure 1.16: Magnetic induction on a coil radial-vertical section in tokamak configuration. The coordinate present on the axes are not representative of the position of the coil with respect to the origin, but simply indicate the dimension of the section.

More detailed results are reported in the next section comparing them,

for verification purposes, with the results obtained in ENEA.

### 1.6.3 Benchmarking

In order to verify the code the results have been benchmarked with the results obtained with OPERA [28], both for what concerns the self field [31] and the overall field generated in tokamak configuration [31]. The ENEA results are representative of the magnetic induction evaluated at the center of each cable. The comparison has been carried out along some specific directions. For what concerns the radial direction the induction has been compared with ENEA results along the sixth, eighth and tenth pancake, being aware of the fact that they are also representative of the other half of the section due to the symmetry that is expected to exist in the results, while for what concerns the toroidal direction first, fifth and ninth turns have been used for benchmarking purposes. In the following figures the result comparisons for the self field are shown, in Figure 1.17 in toroidal and in Figure 1.18 in radial direction.

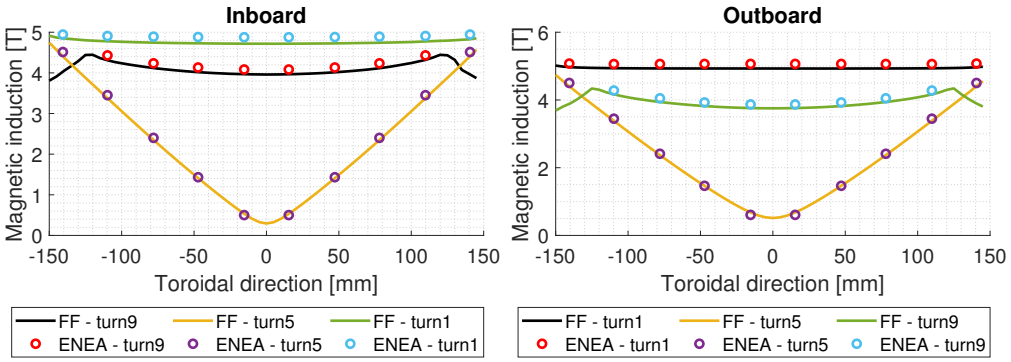


(a) (b)

Figure 1.17: Benchmark between FreeFem++ and ENEA results in toroidal direction at equatorial inboard (a) and outboard (b) coil cross section respectively.

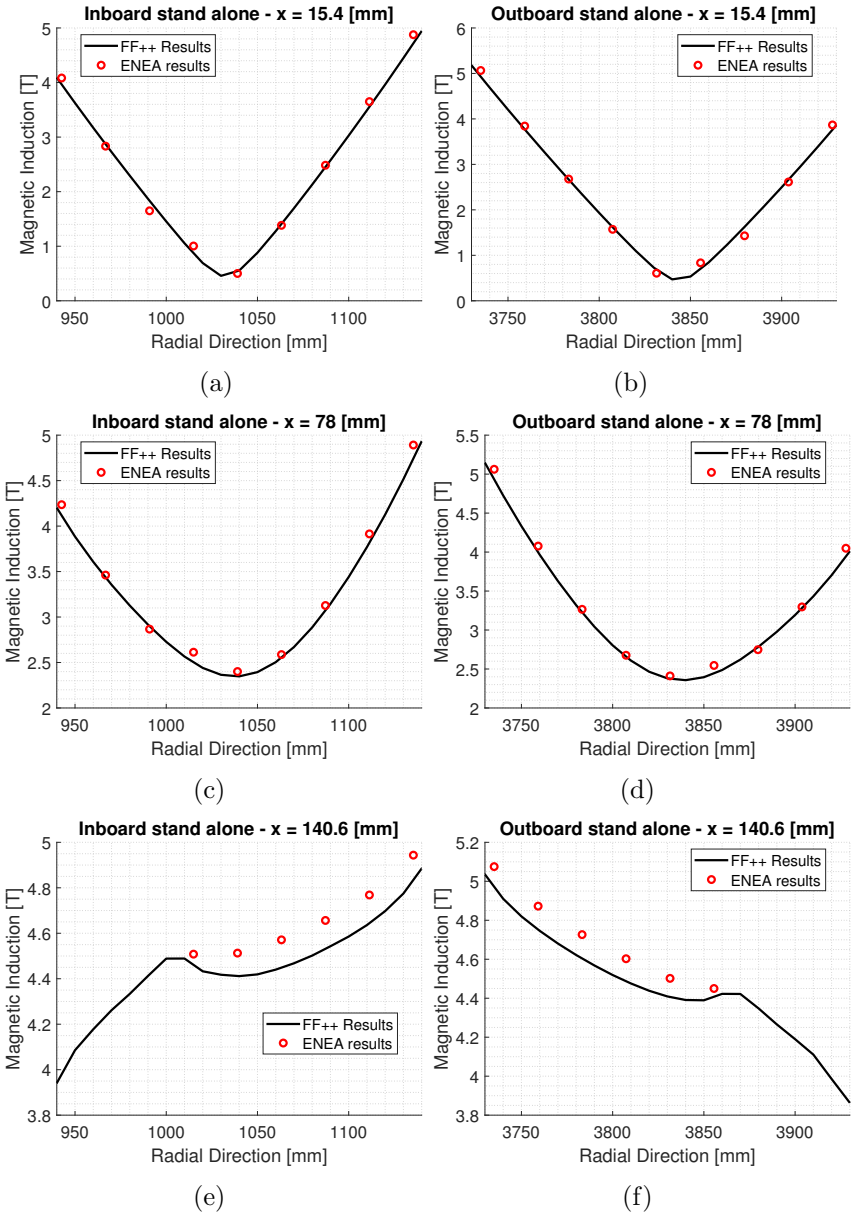


Figure 1.18: Benchmark between FreeFem++ and ENEA results in radial direction at sections: equatorial inboard pancake 6 (a), equatorial outboard pancake 6 (b), equatorial inboard pancake 8 (c), equatorial outboard pancake 8 (d), equatorial inboard pancake 10 (e) and equatorial outboard pancake 10 (f)

The very same locations are used for the benchmarking of the full machine simulation, as it is possible to see in figure 1.19 for what concern the toroidal and in figure 1.20 for the radial direction.
The obtained results are fully comparable with those obtained at ENEA with a maximum discrepancy of a tenth of Tesla, a difference considered to be acceptable between the two tools.

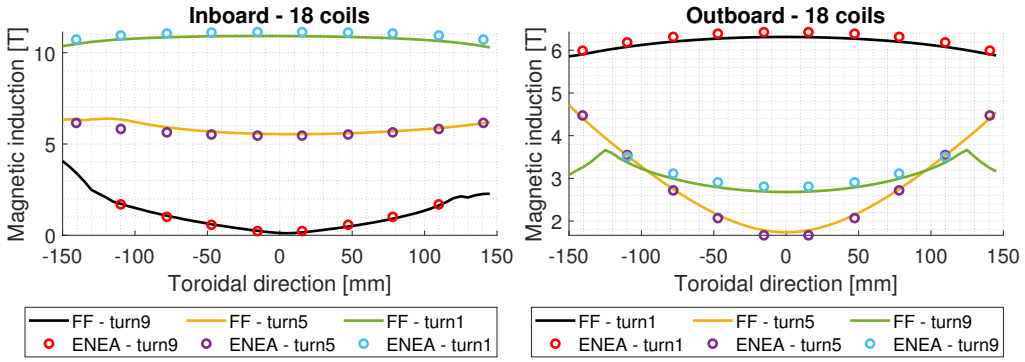


(a) (b)

Figure 1.19: Benchmark between FreeFem++ and ENEA results in full machine simulation in toroidal direction at equatorial inboard (a) and outboard (b) cross section respectively.

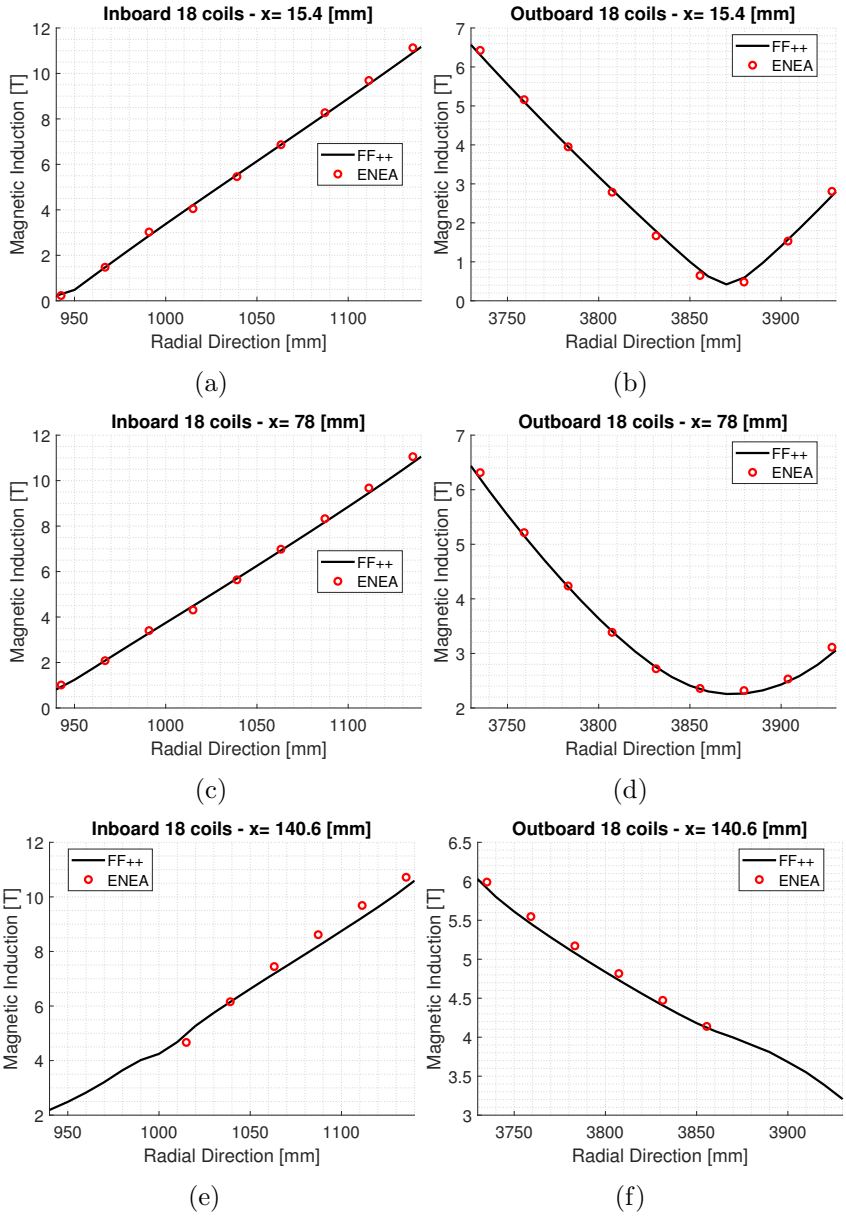


Figure 1.20: Benchmark between FreeFem++ and ENEA results in full machine simulationin radial direction at sections:equatorial inboard pancake 6 (a), equatorial outboard pancake 6 (b), equatorial inboard pancake 8 (c), equatorial outboard pancake 8 (d), equatorial inboard pancake 10 (e) and equatorial outboard pancake 10 (f)

# Chapter 2

# Electrodynamic models and eddy current computation

## 2.1 Introduction

The eddy current computation has a fundamental role in the electrodynamic modeling of any kind of magnetic system due to the power deposition in the structural materials caused by Joule effect. In the case of superconducting magnets this analysis is even more important since the superconductive state is preserved only below certain temperature limits, depending on the material and on the working conditions, that can be overcome in case of excessive Joule power deposition originating quench phenomena into the coil. The origin of the eddy current is the variation of the magnetic induction either due to the normal pulsed operations typical of a tokamak or due to off - normal current transients such as the fast discharge. The phenomenology of the generation of eddy currents is described by two additional equations that will be coupled with the Ampère law (equation 1.1) already discussed in the magnetostatic case: the Faraday law ( equation 2.1) and the Ohm law (equation 2.2).

$$\nabla \times \overrightarrow{E} = -\frac{\partial \overrightarrow{B}}{\partial t} \tag{2.1}$$

$$\overrightarrow{J} = \sigma \overrightarrow{E} \tag{2.2}$$

These equations must be properly coupled with Ampère law to obtain the equation representative of the problem. In literature several techniques are

adopted and described [8], in this work the A-formulation has been adopted for the magneto-dynamic analysis too. This formulation is valid, ensuring the proper gauge on its own, only using edge elements; this has been ensured making use, in FreeFem++, of Edge03d elements.
From the practical point of view the A-formulation introduces the definition of the magnetic vector potential in the Faraday equation obtaining a direct correlation between the electric field and the magnetic vector potential itself (equation 2.3).

$$\nabla \times \overrightarrow{E} = -\frac{\partial}{\partial t}(\nabla \times \overrightarrow{A}) \tag{2.3}$$

Given that the curl operator is not depending on time, it can be moved outside the time derivative and simplified. Under the assumption that the gradient of the electric potential is always equal to zero, the electric field can be directly expressed as a function of the magnetic vector potential (equation 2.4).

$$\overrightarrow{E} = -\frac{\partial \overrightarrow{A}}{\partial t} \tag{2.4}$$

In presence of a conductive material, such as the magnets structures, the electric field is generating, according to Ohm law (equation 2.2), eddy currents that can now be expressed directly as a function of the magnetic vector potential too (equation 2.5).

$$J_{eddy} = -\sigma \frac{\partial \overrightarrow{A}}{\partial t} \tag{2.5}$$

Recalling the Ampère law (1.1), at the left hand side a current is imposed as a driver. In the magnetostatic case, that current was the current flowing into the coil and the driver of the problem. In the magneto-dynamic analysis both the driver current and the eddy current must be considered while writing down the Ampère law, obtaining the following equation (equation 2.6).

$$\nu \nabla \times (\nabla \times \overrightarrow{A}) = \overrightarrow{J}_D - \sigma \frac{\partial \overrightarrow{A}}{\partial t} \tag{2.6}$$

This equation is valid in the entire domain once the properties are well defined and the driver current is a divergence free vectorial field. In the framework of eddy current computation the wave behavior of the Maxwell equations is

neglected, neglecting itsimpact with respect to that of the eddy currents.
Equation 2.6 is fully representative of the problem analyzed and using a proper weighting function $\overrightarrow{v}$ it is possible to obtain the Galerkin equation to be solved with FE method (2.7).

$$\int_{\Omega} \nu \nabla \times \overrightarrow{v} \cdot \nabla \times \overrightarrow{A} d\Omega + \int_{\Omega} \sigma \overrightarrow{v} \frac{\partial \overrightarrow{A}}{\partial t} d\Omega = \int_{\Omega} \overrightarrow{J}_D \cdot \overrightarrow{v} d\Omega \qquad (2.7)$$

## 2.2 FreeFem++ model development

The Galerkin equation that has been previously computed (2.7) must be properly translated in FreeFem++ language. The first important thing is to properly subdivide the mesh into the regions representing the different parts of the domain: the winding pack region in which the driver current must be imposed, the conductive structure where the eddy currents are generated and the outside region that is used to close the field lines.
The equation that must be solved is differential both in space and time. For what concerns the spatial discretization, a 3D tetrahedral mesh is uploaded in FreeFem++ for each case studied and the built in FreeFem++ solver assembles on its own the matrix to be used for the solution of the algebraic system representative of each time step of the solution. The time discretization is, otherwise, developed directly in the model making use of the backward Euler method. The Galerkin equation to be solved is therefore discretized in time as reported in equation 2.8 where the superscript $n$ stands for the time step at which the equation is solved and the superscript n-1 stands for the previous time step.

$$\int_{\Omega} \nu \nabla \times \overrightarrow{v} \cdot \nabla \times \overrightarrow{A}^n d\Omega + \int_{\Omega} \sigma \overrightarrow{v} \frac{\overrightarrow{A}^n - \overrightarrow{A}^{n-1}}{\Delta t} d\Omega = \int_{\Omega} \overrightarrow{J}_D \cdot \overrightarrow{v} d\Omega \qquad (2.8)$$

The solution at the time step n-1 is known and so it can be moved at the right hand side of the equation making it belong to the known term vector (equation 2.9).

$$\int_{\Omega} \nu \nabla \times \overrightarrow{v} \cdot \nabla \times \overrightarrow{A}^n d\Omega + \int_{\Omega} \sigma \overrightarrow{v} \frac{\overrightarrow{A}^n}{\Delta t} d\Omega = \int_{\Omega} \overrightarrow{J}_D \cdot \overrightarrow{v} d\Omega + \int_{\Omega} \sigma \overrightarrow{v} \frac{\overrightarrow{A}^{n-1}}{\Delta t} d\Omega \qquad (2.9)$$

This last equation is than translated in FreeFem++ language, the matrix assembly is automatically performed by the software and the obtained algebraic system is solved by MUMPS (MUltifrontal Massively Parallel Solver), that is a package for solving systems of linear equations with a direct method which performs a Gaussian factorization [10].
The solution of the algebraic system provides an approximation of the magnetic vector potential that can be used to reconstruct all the other relevant unknowns such as the evolution of the magnetic field, but mainly the eddy currents and, consequently, the deposited Joule power. The eddy currents are evaluated simply using equation 2.5, while the Joule power is evaluated with the following equation (2.10).

$$P_{Joule} = \int_{\Omega_c} \frac{1}{\sigma} \cdot \overrightarrow{J}^2_{eddy} d\Omega \tag{2.10}$$

Notice that the integral is evaluated only on the fraction of the domain in which the eddy currents are developed and so in the conductive region of the structures.
For what concerns the computational grid, the tool has been interfaced with an external mesher in order to improve the flexibility. FreeFem++ can easily generate meshes for simple geometries making use of the parametric geometry definition that is built in the language, but when the geometries start becoming more complicated the mesh generation is particularly uncomfortable. For this reason the connection between FreeFem++ and the external mesher Gmsh 4.8.1 [11] has been adopted. Gmsh has been adopted as external mesher between all the possible choices for the extremely high compatibility with FreeFem++ language.
Gmsh is an open source three-dimensional finite element mesh generator with possibility to generate geometries thanks to the built-in CAD engine (OpenCASCADE [32]) or importing directly the CAD of the geometry in several different formats; the suggested format to be adopted in this tool is the .step, even if that is not mandatory.
The mesh is generated in Gmsh thanks to the Delaunay algorithm, obtaining tetrahedral meshes compatible with the FreeFem++ structure.[11]

## 2.3 Benchmarking of the tool in simple problems

In order to verify the developed tool in condition relevant for real-case applications, it has been tested in simple problems in order to benchmark it against available solutions and against results obtained with other tools. In this case two problems have been considered for this purpose, the first for which several literature results are available and the second for which the tool as been benchmarked against a state of the art FE commercial code.
The first case is the TEAM 4 problem (The Felix brick) [9] that is relevant to evaluate the potentiality of the tool even with the current driver set to zero and using as a driver externally imposed time varying magnetic fields, while the second is the analysis of a circular conductor leading a time varying current surrounded by a stainless steel jacket in which eddy currents can be generated.

### 2.3.1 Benchmark 1 - The Felix brick

In this problem a rectangular aluminum brick with a rectangular hole through it is placed in a uniform magnetic field that is normal to the holed faces and decreases exponentially in time. Eddy currents are generated in the brick and a certain Joule power is deposited too. For benchmarking purposes the Joule power evolution and the magnetic field profiles at different time instants are evaluated and compared with literature results [9].
The brick in figure 2.1 is made of aluminum alloy 6061 of electrical resistivity $\rho = 3.94\mu\Omega cm$, the main dimensions are reported in figure 2.1 too, while the hole is centered on the large face and its dimensions are $0.0889m \times 0.0381m$.

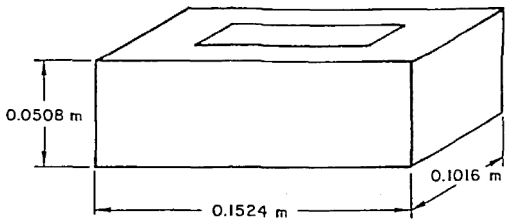


Figure 2.1: Domain of the reference problem in [9]

The applied magnetic field is oriented along z-axis and uniform in space, decaying in time with the law provided in equation 2.11.

$$B_z = B_0 \cdot e^{-\frac{t}{\tau}} \tag{2.11}$$

where $B_0 = 0.1[T]$ and $\tau = 0.0119[s]$.
The solution of the problem has been obtained using the developed electro - magnetic tool and the comparison with the results proposed in [9] is performed on the Joule power evolution and on the magnetic induction profile on the middle plane of the brick at different time instants (4 [ms], 8 [ms], 12 [ms], 16 [ms], 20 [ms]), see figure 2.2 and 2.3.

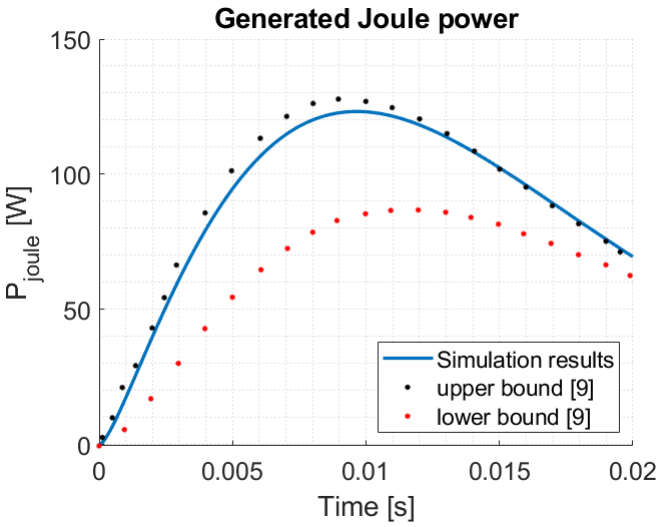


Figure 2.2: Comparison between literature results [9] and simulation outcomes for the Joule Power

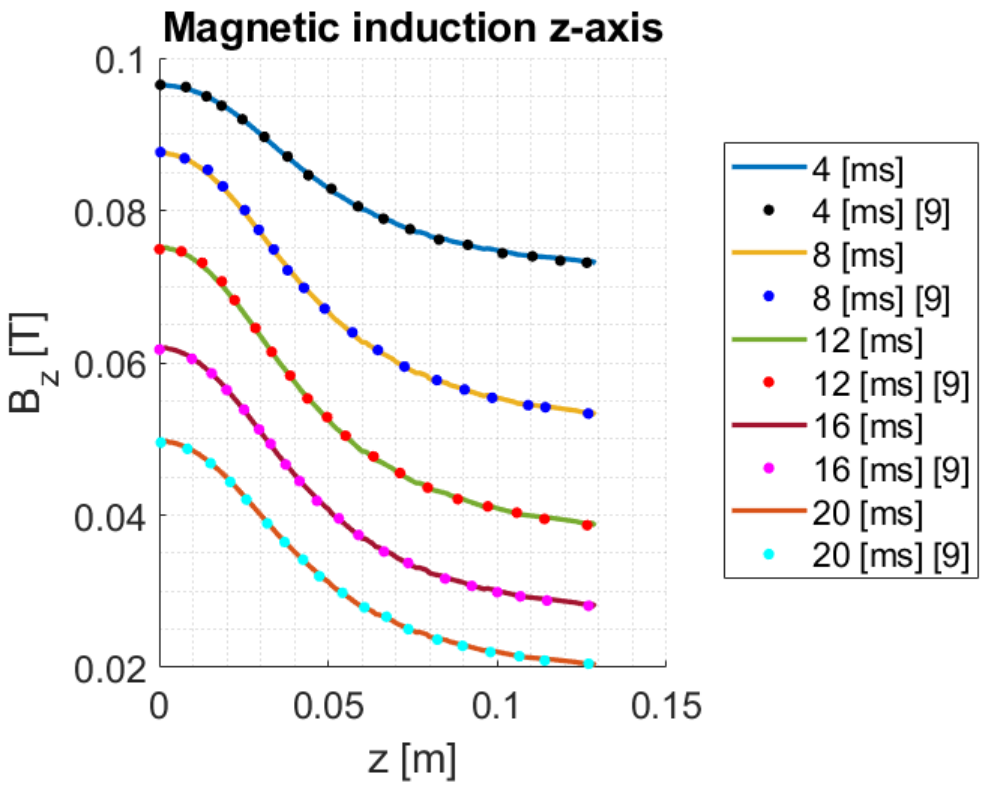


Figure 2.3: Comparison between literature results [9] and simulation outcomes for the Magnetic induction

As it is possible to observe the comparison with the literature results for what concerns the magnetic induction is extremely accurate; the power deposition results differs consistently between the different benchmarked codes of [9], but the results of the developed tool are fully comparable with the interval detected in the paper.

### 2.3.2 Benchmark 2: a simplified coil

For benchmarking purposes another simple case has been considered trying to move closer to the real case applications. The geometry considered in this is a simple circular conductor with a steel jacket around in which eddy current are generated due to the time variation of the driver current flowing in the conductor. The dimensions and the relevant physical properties are reported in the following table (Table 2.1).

Table 2.1: Dimensions, data and relevant physical properties adopted in the benchmark test case.

| **Quantity** | **Description** | **Value** | **Unit** |
|---|---|---|---|
| R | Coil radius | 1.0 | [m] |
| $r_c$ | Conductor radius | 0.10 | [m] |
| $r_j$ | Jacket radius | 0.13 | [m] |
| $\mu$ | Magnetic permeability | $4\pi \cdot 10^{-7}$ | [H/m] |
| $\sigma_j$ | Jacket electric conductivity | $1.12 \cdot 10^7$ | [S/m] |
| $J_0$ | Initial current density | $1.0 \cdot 10^4$ | $[A/m^2]$ |

The above described geometry is presented in Figure 2.4 that shows the CAD model of this geometry. This is relevant since the benchmark test has been also used to demonstrate the flexibility of the tool that is able to handle any kind of geometry simply importing the CAD in the above mentioned mesher (Gmsh 4.8.1).

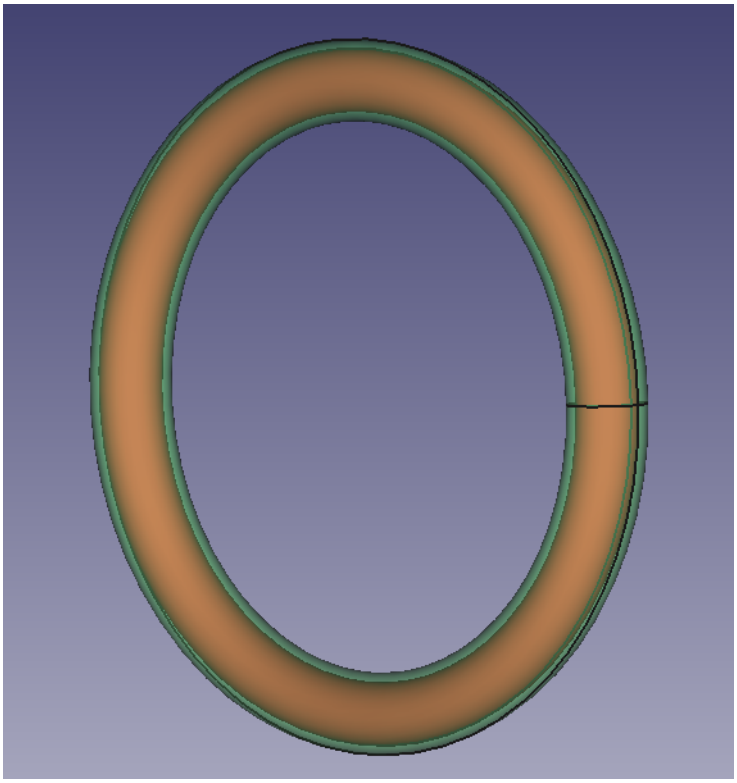

Figure 2.4: Benchmark test geometry. In orange the conductor, in green the jacket

The current density evolution is considered to be exponentially decreasing according to the equation 2.12.

$$J(t) = J_0 \cdot \exp(-t) \tag{2.12}$$

For stability reasons it is preferable not to impose approximated initial conditions to the algorithm and for this reason, even if interested only on the dump of the current, the simulation is required to load the current starting from zero up to the initial condition, reach steady state and finally analyze the current dump. This clearly makes the computation longer, but assures proper initial conditions for the dump. By the way the computational time lost for the loading of the current can be reduced making use of a larger time step in the analysis, given that whatever happens before the dump is not requiring detailed results, but only exists to provide proper initial conditions.

Following the very same procedure as described in the introductory part, the evolution of the Joule power deposited in the jacket is evaluated and compared with the results of the same problem obtained with the commercial FE software COMSOL [29]. The results are shown in Figure 2.5.

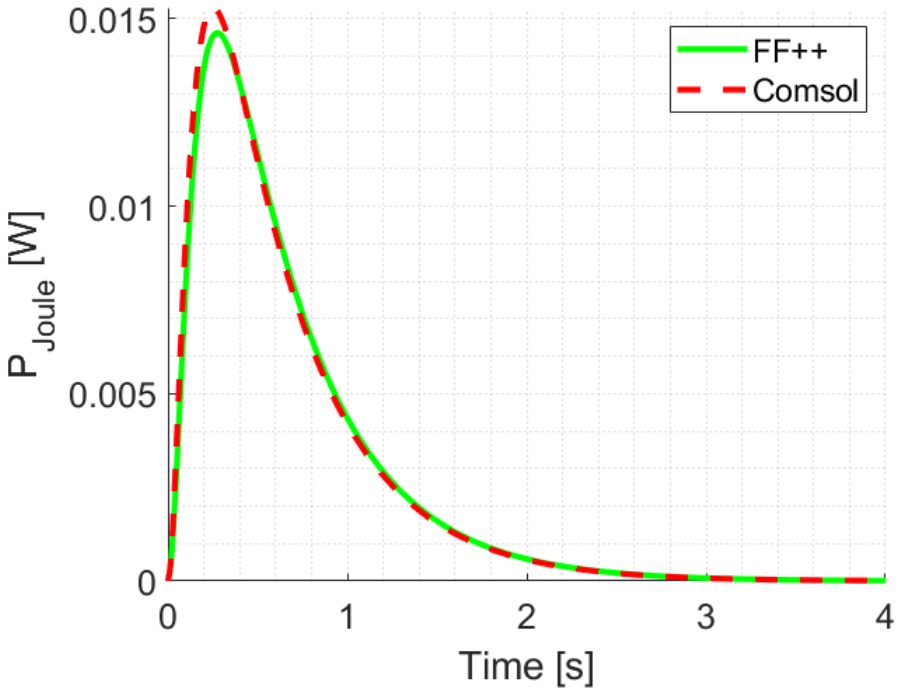


Figure 2.5: Comparison between FF++ and COMSOL results.

To be sure that the tool is, by the way, solving the equations properly, also a grid independence study has been performed for this benchmark test; the convergence of the algorithm is shown in figure 2.6, where the mesh adopted is also highlighted. The choice of the mesh is, in this case, mainly focused to the speed up of the computation and not on the extreme precision of the results.

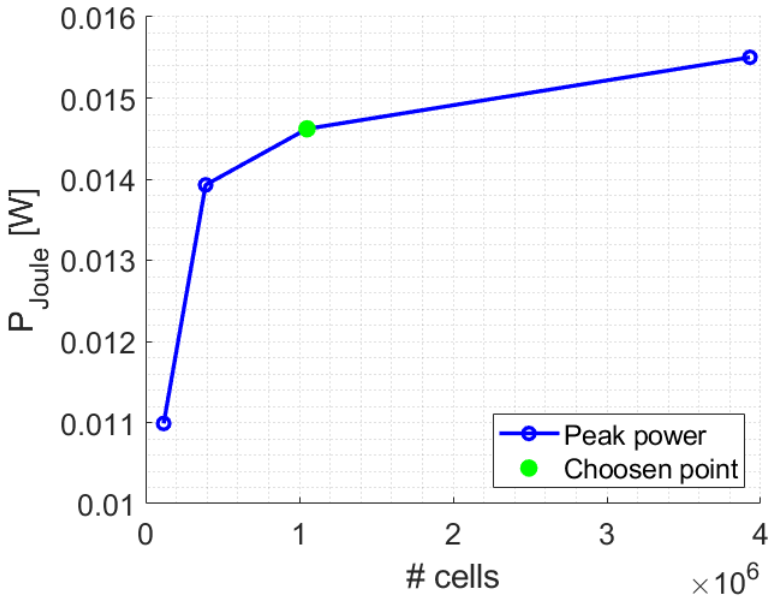


Figure 2.6: Grid independence study for the benchmark test.

The two benchmark examples that are shown here have been developed in order to demonstrate that the tool is able to work both in the case in which the variation of the magnetic field is externally imposed (Felix brick example) and in the case in which the variation of the magnetic field depends on the variation of a current that is imposed in a conductive region belonging to the computational domain. By the way this proposed benchmarking needs to be integrated with a detailed validation in the real case application of the tool against the experimental data that are expected to be available in the close future.

## 2.4 Introduction of the parallel computing

As already described, the problem that is being solved with this tool is a fully 3D transient problem that is requiring huge amounts of computational resources. To better use these resources the parallel computing has been introduced in the tool. The parallel computing is the application of two or more processing units to solve a single problem [12]. FreeFem++ is interfaced

with PETSc library which also includes some toolkit that can be used for the parallelization of the code, such as domain decomposition methods (e.g. HPDDM) and parallel solvers. The idea is that the domain is decomposed and each processor should solve the problem in a single part of the domain. This would speed up the computation allowing to solve the problem in finer meshes.
For what concerns the FreeFem++ implementation of the parallel code, the methodology is simplified by the presence of the above mentioned dedicated libraries that include the commands that directly parallelize the problem, decomposing the geometry and assigning each subsection of the domain to the dedicated processor without asking the user to code communication strategy between different nodes. Thanks to this parallelization strategy the solution of the problem from the coding point of view is, for what concerns the core business, the same as solving the problem in a sequential way. The main differences arise during the post processing phase since the results, in order to be manipulated to obtain the desired outcome, need to be transported from the local fragmented mesh to the original uniform one. Doing that it is fundamental to cut the results linked with the so called ghost elements that are cells belonging to more than one fragment of the mesh used by the solver to assure proper communication between the different mesh sections. This procedure must be performed by means of the so called partition of unity that is done thanks to some dedicated commands included in the PETSc library.
Once the partition of unity is performed, the final results manipulation and the outcome storage is sequentially performed only on the processor number zero.
The parallel tool has not been directly adopted in this work due to the impossibility of exploiting enough computational resources, but is considered a key point for the future development of the tool, both in improving the results and in assessing the errors of the simulation thanks also to the future comparison with experimental results.
The translation of the tool from sequential to parallel has been performed taking as main reference the Professor Pierre Jolivet lectures at the 2020 FreeFem days [24].

# Chapter 3

# Real case application: DTT TF electrodynamic analysis

The tool that has been developed can find wide range of application during the design of superconducting magnets for fusion machines, both for design purposes and performance assessment, but also, potentially, to perform predictive simulations. In this work a real case application on a fusion machine is proposed simulating the behavior of the DTT toroidal field (TF) coil. The transient that has been chosen as test case is the fast current discharge in a single TF, aiming to represent the experimental campaign that will be held at the DTT cold test facility in the following few years. The fast discharge is the exponential dump of the current from its nominal value. This transient of the current is represented by the following equation (3.1).

$$\overrightarrow{J}(t) = \overrightarrow{J_0} \cdot e^{-\frac{(t-t_0)}{\tau}} \tag{3.1}$$

In this equation $J_0$ is the steady state current density value, $t_0$ the time at which the dump begins and $\tau$ is the transient time constant. The steady state current density is evaluated using equation 3.2 and the value of the missing data is reported in Table 3.1.

$$\overrightarrow{J_0} = \frac{I_0 \cdot N_c}{A_{WP}} \cdot \hat{n} \tag{3.2}$$

Table 3.1: Relevant data for the evaluation of the current dump transient during fast discharge.

| Quantity | Description | Value | Unit |
|---|---|---|---|
| $I_0$ | Steady state cable current | 42.5 | [kA] |
| $N_c$ | Number of turns in the WP | 84 | [-] |
| $A_{WP}$ | WP cross section | $6.216532 \cdot 10^{-2}$ | $[m^2]$ |
| $\tau$ | Transient time constant | 5.0 | [s] |

## 3.1 Geometry and materials

In addition to the geometry of the winding pack (WP) of the DTT TF that has been already described in the first chapter, the information related to the bulky metallic structures must be included given that eddy currents are generated there. The geometry of DTT TF structure is extremely complicated including a lot of components that can be neglected for the purpose of the work (e.g PF support, gravity support, Helium loop components). The real detailed geometry is shown in figure 3.1.

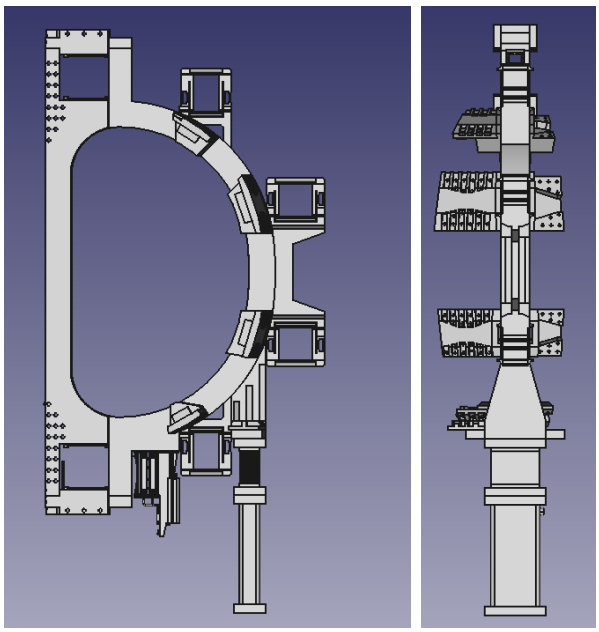

Figure 3.1: Detailed geometry of the DTT TF structures [23]

All these additional details are supposed not to provide relevant contribution to the final result since the eddy currents are mainly generated in the bulky structure close to the WP. For this reason a simplified version of the structure geometry has been proposed only considering the bulky metallic material constituting the main body of the structure as shown in figure 3.2. The geometry used for the computation is extremely simplified, but it keeps the relevant information for the computation, such as the dimensions and the different cross section at the inboard and at the outboard (inboard trapezoidal section, outboard rectangular section).

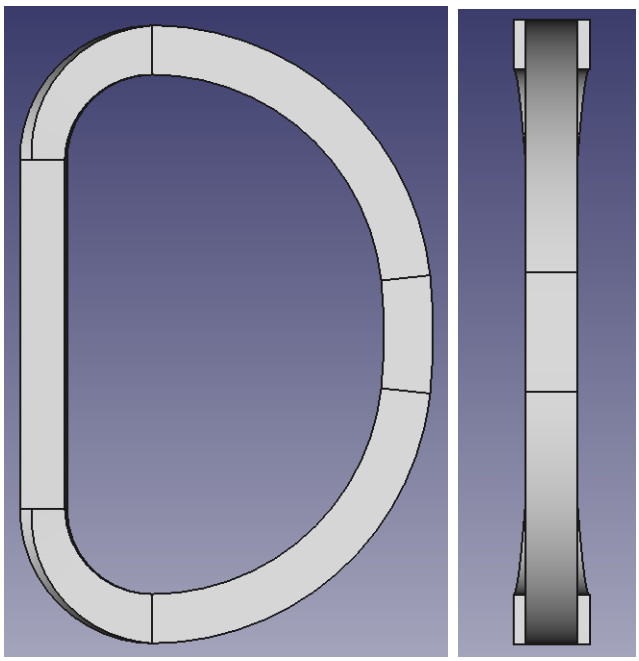

Figure 3.2: Simplified geometry of the DTT TF structures

Also the materials and their properties have an important role in the results of the simulation. The superconductive cables are made of $Nb_3Sn$, while the structures are built with stainless steel. Looking at the equation to be solved the relevant properties are the magnetic permeability of all the materials and the electrical conductivity of the stainless steel, fundamental for the evaluation of eddy currents and the power that they generate.
For what concerns the magnetic permeability, it has been assumed to be

constant and uniform all over the domain and equal to the vacuum one.

$$\mu = 4\pi \cdot 10^{-7}[H/m] \tag{3.3}$$

The electrical conductivity of the steel is depending on the temperature of the material itself, but, since no thermal feedback exists, at present, the property is assumed to be constant all along the transient and equal to the value at 4.5 [K] that is, approximately, the initial temperature of the magnet. The conductivity reported below is taken from [21] at the reference temperature.

$$\sigma = 2.0 \cdot 10^{6}\,[S/m] \tag{3.4}$$

Possible future development of the tool may include the temperature dependence of the electrical conductivity in order to assess its impact on the final result or, in order to at least try to assess the influence of the temperature variation of the structures, some sensitivity analysis varying parametrically the value of the conductivity and observing the variation of the final results.

## 3.2 Simulation setup

The objective of the simulation is, as mentioned above, the analysis of a fast current discharge starting from the steady state nominal value of current with an exponential dump described in equation 3.1. For numerical stability the simulation is performed not only including the dump, but following the current density evolution shown in figure 3.3.

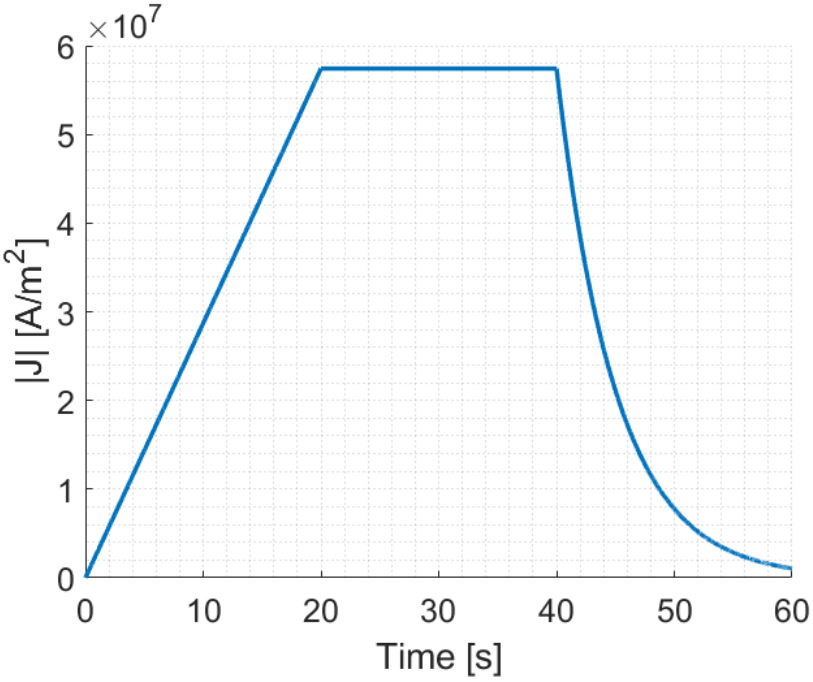


Figure 3.3: Module of the current density during the simulation

This time evolution has three big advantages. The first one is that in such a way it is possible to impose an exact initial condition. Indeed having no current flowing in the coil at the beginning of the simulation all the components of the magnetic potential, that is the problem unknown, are exactly set to zero (equation 3.5).

$$\overrightarrow{A}(t=0) = [0,0,0]; \tag{3.5}$$

Moreover the presence of a real current rump up avoids to have nonphysical spikes on the final relevant result, the power deposition, given by the jump of the solution that would be computed in case of discontinuity in the definition of the driver.
Finally the steady state section is numerically helpful since the solution has the time to stabilize to the proper steady state value, so that the dump surely starts from the proper initial condition.
The dump has been analyzed for a time interval of 20 [s], i.e. four time the time constant, so that the driver is decreased of almost two orders of magnitude with respect to the initial value. Since in the last part of the transient

the eddy currents are expected to be proportional to the driver and the deposited power to be proportional to the second power of the eddy current, this means that after 20 [s] the deposited power is expected to be four orders of magnitude smaller that its peak; that is considered to be small enough to stop the simulation.
At the artificial boundaries homogeneus boundary conditions can be assumed [8] and so it is possible to impose that:

$$\overrightarrow{B} \cdot \hat{n} = 0 \qquad on\ \Gamma_n \tag{3.6}$$

Introducing the magnetic vector potential the boundary condition is translated in the following (equation 3.7):

$$\nabla \times \overrightarrow{A} = 0 \qquad on\ \Gamma_n \tag{3.7}$$

This condition, in presence of edge finite elements is automatically satisfied by an homogeneous condition.
As already mentioned in the previous chapter, the problem is solved with the direct solver MUMPS. For simulations not excessively heavy the problem is solved sequentially loading the sequential library of MUMPS, that however borns as a parallel solver and so is perfectly usable also for the parallel solution with a simple adjustment of the code loading the macroddm and PETSc libraries directly in FreeFem++.

## 3.3 Mesh generation

The geometry has been generated by means of an open source CAD editor (FreeCAD [33]) and saved into a format (.step) suitable to be imported in the open source mesher Gmsh that is adopted in the tool. In order to complete the mesh in addition to the structures and the winding pack also the external air must be meshed. In the selected case with the analysis of a single TF (self field) the external air is represented by a sphere. The radius of the sphere is set to $R = 10[m]$. The grid independence analysis has been performed in order to choose the most proper mesh refinement, see below.
In order to be fully compatible with FreeFem++ the mesh has been developed only including tetrahedral elements that have been generated by means of the Delaunay algorithm already implemented in the mesher.

In the following figures an example of mesh is shown: in the first one (figure 3.4) an overview of the overall mesh, including the external world, is reported in order to show the position of the magnet, while the second (figure 3.5) shows a detail of the mesh highlighting the different refinement that has been adopted between the winding pack and the structures, with a much more refined mesh in the structures where the eddy currents, subject of the study, are generated.

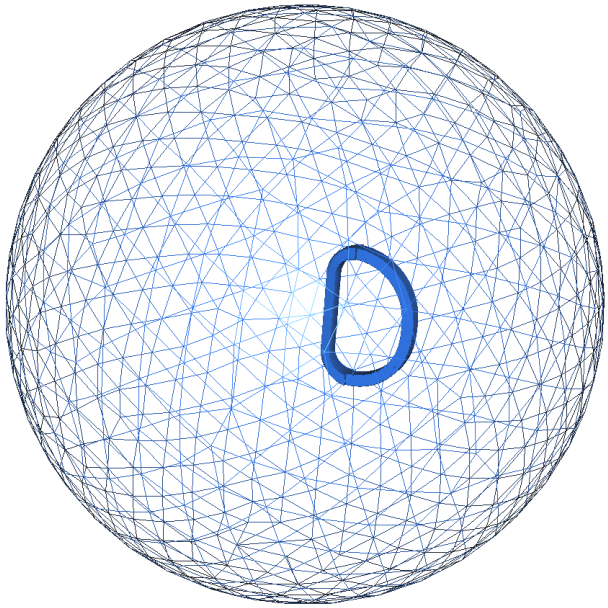

Figure 3.4: Mesh adopted for eddy current computation

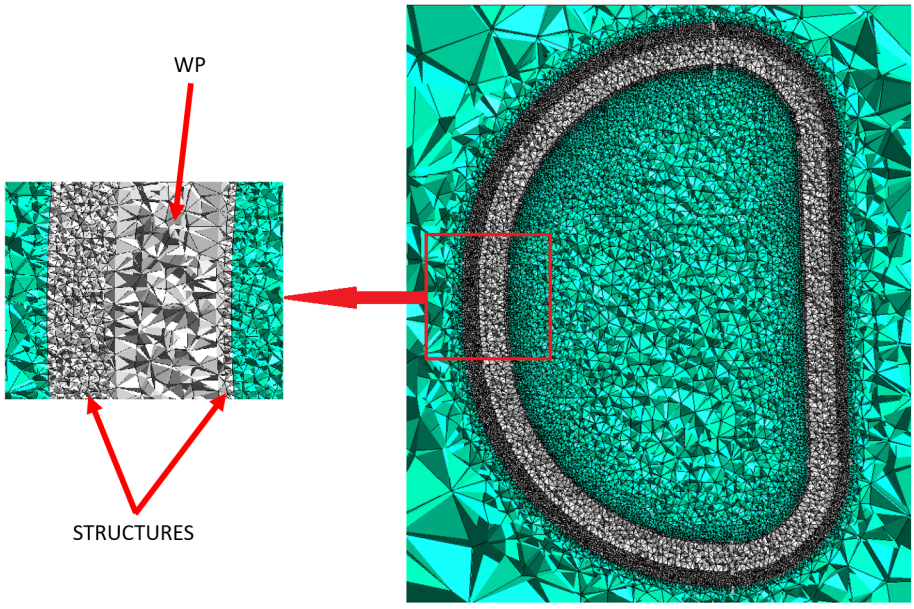


Figure 3.5: Detail of the mesh in correspondence of structures and WP

### 3.3.1 Grid independence analysis

To assure that the equations are actually properly solved a grid independence analysis has been performed analyzing in a parametric way the value of the peak of power evolution. The first parameter that has been considered is the refinement of the external environment. The cell size has been fixed, at the boundary, at four different values keeping the mesh of structures and winding pack unchanged. The mesh characteristics are summarized in the following table (Table 3.2) and the convergence of the computation is shown in the plot in figure 3.6.

Table 3.2: Mesh characteristics (external world refinement). The average cell size is directly imposed in the different regions in the mesher thanks to dedicated field functions

| **Mesh** | **WP cell size [m]** | **Steel cell size [m]** | **Air cell size [m]** | **cell number** |
|---|---|---|---|---|
| 1 | $4.0 \cdot 10^{-2}$ | $2.5 \cdot 10^{-2}$ | 2.5 | $7.35 \cdot 10^{5}$ |
| 2 | $4.0 \cdot 10^{-2}$ | $2.5 \cdot 10^{-2}$ | 2.0 | $8.85 \cdot 10^{5}$ |
| 3 | $4.0 \cdot 10^{-2}$ | $2.5 \cdot 10^{-2}$ | 1.5 | $1.03 \cdot 10^{6}$ |
| 4 | $4.0 \cdot 10^{-2}$ | $2.5 \cdot 10^{-2}$ | 0.75 | $1.75 \cdot 10^{6}$ |

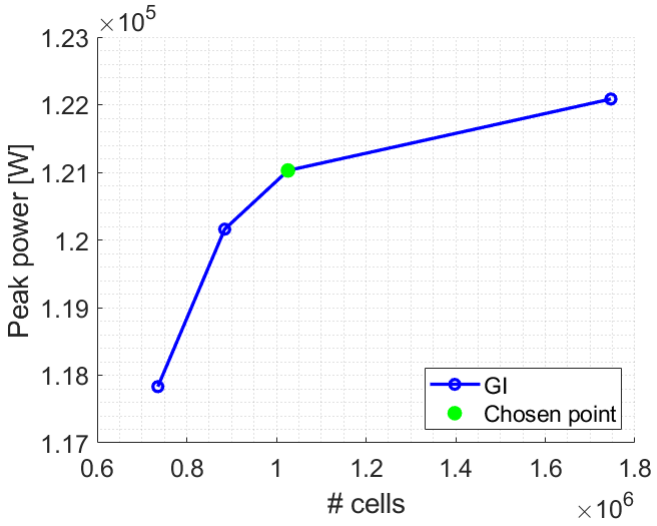


Figure 3.6: Grid independence analysis (external world refinement). Highlighted in green the selected grid.

The convergence of the solution is demonstrated and the chosen cell size for the external world is the one highlighted in green since it is the best compromise between computational resources requirement and accuracy, given that the difference with respect to the finer mesh is smaller than 1%.
The same analysis has been then performed varying the refinement of the structure that is the more delicate region, in which the eddy currents are generated. The WP is not requiring particular attention in the refinement since no relevant issue of the solution is expected to arise there.
The mesh characteristics are reported in Table 3.3 and the convergence of

the computation is shown in figure 3.7.

Table 3.3: Mesh characteristics (structures refinement). The average cell size is directly imposed in the different regions in the mesher thanks to dedicated field functions

| **Mesh** | **WP cell size [m]** | **Steel cell size [m]** | **Air cell size [m]** | **cell number** |
|---|---|---|---|---|
| 1 | $4.0 \cdot 10^{-2}$ | $3.5 \cdot 10^{-2}$ | 1.5 | $5.30 \cdot 10^{5}$ |
| 2 | $4.0 \cdot 10^{-2}$ | $2.5 \cdot 10^{-2}$ | 1.5 | $1.03 \cdot 10^{6}$ |
| 3 | $4.0 \cdot 10^{-2}$ | $2.0 \cdot 10^{-2}$ | 1.5 | $1.52 \cdot 10^{6}$ |
| 4 | $4.0 \cdot 10^{-2}$ | $1.5 \cdot 10^{-2}$ | 1.5 | $3.17 \cdot 10^{6}$ |
| 5 | $4.0 \cdot 10^{-2}$ | $1.0 \cdot 10^{-2}$ | 1.5 | $8.26 \cdot 10^{6}$ |

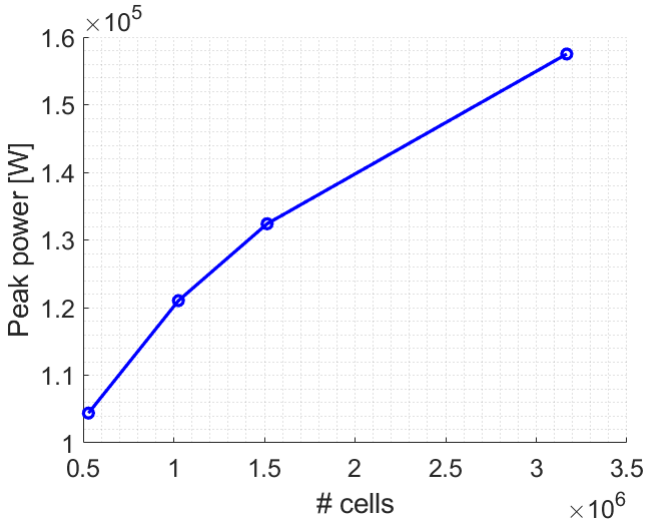


Figure 3.7: Grid independence analysis. Structure refinement.

The selected grids that have been tested are not enough to reach convergence, even if the convergent behavior is clearly observed. This is due to the limited computational resources available at present, but, as mentioned, the tool is able to work with parallel computing and so, in the future when more computational resources will be easily available this analysis can be improved providing estimations on the error that has been committed using as input for the 4C code the outcome of the most refined grid presented here.

## 3.4 Time convergence analysis

When a transient simulation is performed, the convergence of the time marching algorithm must be verified too. The analysis presented here is not demanding a very fine time discretization all along the transient since the time constant is sufficiently big, but as already observed the relevant outcome (power deposited by eddy currents) shows a peak just after the beginning of the current dump. For this reason that part of the transient requires to be sufficiently refined in order to properly resolve the peak. Therefore a 2 seconds time interval in which the peak is expected to appear has been differently refined in order to assess the convergence of the time marching algorithm following the refinement detailed in Table 3.4.

Table 3.4: Time convergence analysis. Time refinement

| **Refinement** | **dt [s]** | **Interval time step** | **Power Peak [W]** | **Energy [kJ]** |
|---|---|---|---|---|
| 1 | 0.1 | 20 | $1.210 \cdot 10^5$ | 364.7 |
| 2 | 0.05 | 40 | $1.238 \cdot 10^5$ | 367.8 |
| 3 | 0.025 | 80 | $1.254 \cdot 10^5$ | 369.7 |
| 4 | 0.01 | 200 | $1.267 \cdot 10^5$ | 370.9 |

The results that have been summarized in the previous table are also shown in the plot of figure 3.8 in which the convergent nature of the time stepping algorithm is clear observing the asintotic behavior of the curve. In the two plots the selected point has been highlighted too. The selected time discretization has been chosen to optimize the computational time, ensuring, by the way, good precision, both the results are less than 1% different with respect to the most refined solution (0.9% difference for what concerns the power peak and 0.3% difference for what concerns the deposited energy). Indeed the selected configuration provides the described precision discretizing the time interval containing the peak in less than half of the time steps, that means decreasing of a factor bigger than two the time required for the simulation of the peak interval.
A possible improvement of the time discretization technique would be the introduction of an adaptation algorithm that would fit the time step according

to the evolution of the transient. This topic can be seen as a possible future development of the tool.

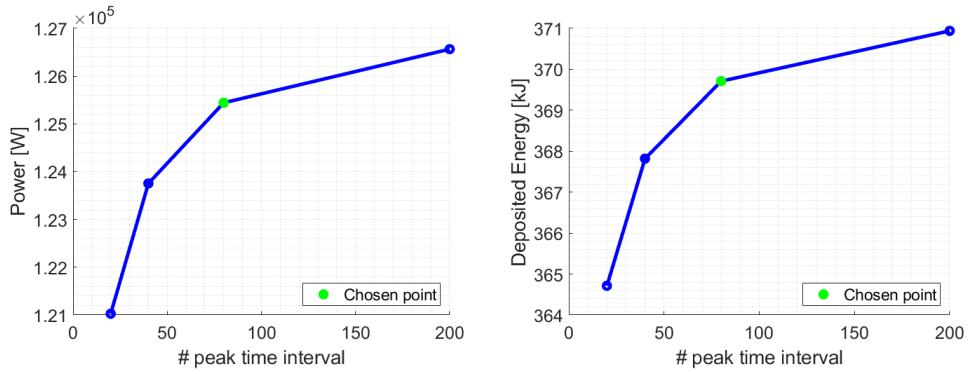


(a) (b)

Figure 3.8: Time convergence analysis. Peak power (a) and deposited energy (b). Highlighted in green the selected time refinement.

## 3.5 Results

The direct result obtained from the solution of the Galerkin equation representative of the problem (equation 2.9) is the magnetic vector potential that, by the way, is not providing on its own relevant information. Its manipulation provides the results that are relevant for this analysis. The developed tool is able to provide the evolution of the magnetic field in each location in the domain and, more important, thanks to subsequent manipulation, the power deposition due to eddy currents. The tool can be freely manipulated to obtain any kind of information related to the power deposition, starting from the local power density to the integral value of the power in the entire volume or only in part of it. This extremely high flexibility is the key point to assure the compatibility of the tool with the 4C code.
Even if not particularly relevant for the evaluation of the power deposition due to eddy currents, the first outcome of the simulation is the time evolution of the magnetic induction. Neglecting the initial rump up of the current and focusing on the relevant part of the transient (the current dump) the magnetic field is expected to decrease monotonically from the initial steady state value, that is the same that has been evaluated with the magnetostatic

tool and that can be seen in figure 1.14, and reaching asintotically zero as the current reaches zero as well. Instead of looking at the local evolution of the magnetic induction, a series of map at different times during the transient has been adopted to show the global evolution of the magnetic induction. In figure 3.9 six maps are reported showing the magnetic induction at the steady state initial value, $0.5\,[s]$, $1.0\,[s]$, $2.5\,[s]$, $5.0\,[s]$ and $10.0\,[s]$ after the beginning of the dump. As expected it is possible to observe the monotonic decrease of the magnetic induction value in all the domain. The color scale has been kept fixed so that it is easier to appreciate the decrease of the magnetic induction.

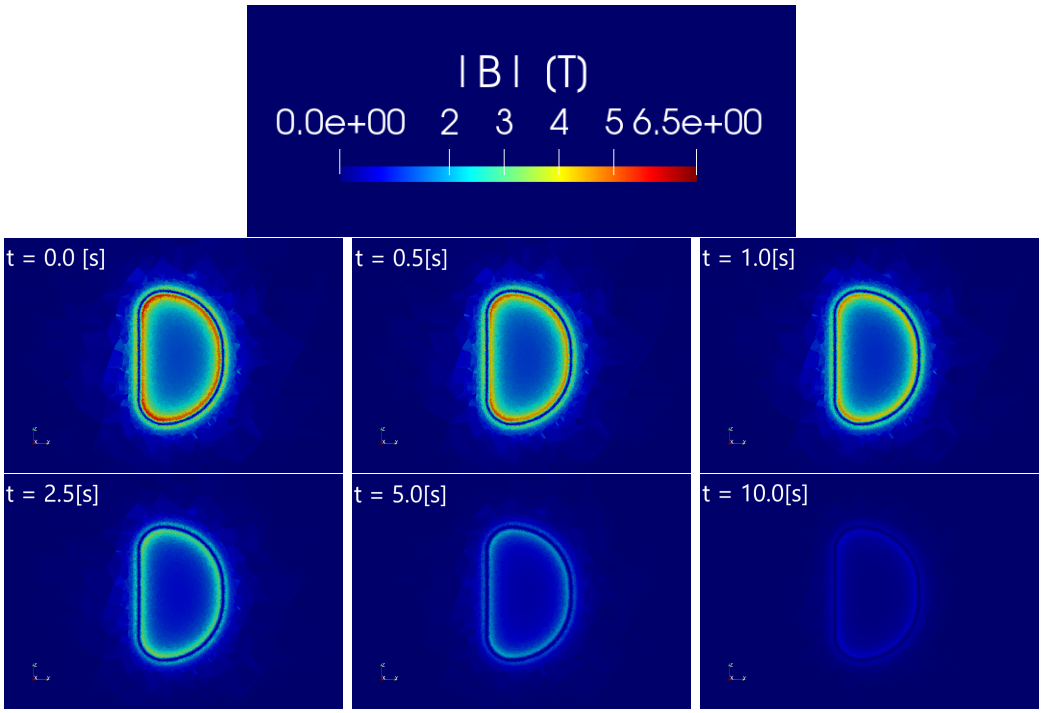


Figure 3.9: Magnetic induction evolution during fast current discharge in DTT TF coil. The time indicated must be intended measured from the dump beginning.

The relevant outcome of this simulation is the power that is deposited in the structures. What is locally evaluated is the power density, but for the purpose of using this information as an input to the 4C cod,e integral infor-

mation are required (the coupling strategy will be explained in detail in the next chapter). The first information that is presented here is the evolution of the overall power that is deposited in the coil structures. This evolution is shown in figure 3.10. The trend is reasonable since it starts from zero, given by the initial steady state current, and then reaches a peak to successively follow an exponential decrease according to the evolution of the driver. The presented plot shows a time axis that is not representing the entire simulated time, but only the part in which the dump occurs, since it is the relevant part for the subsequent steps of the analysis.

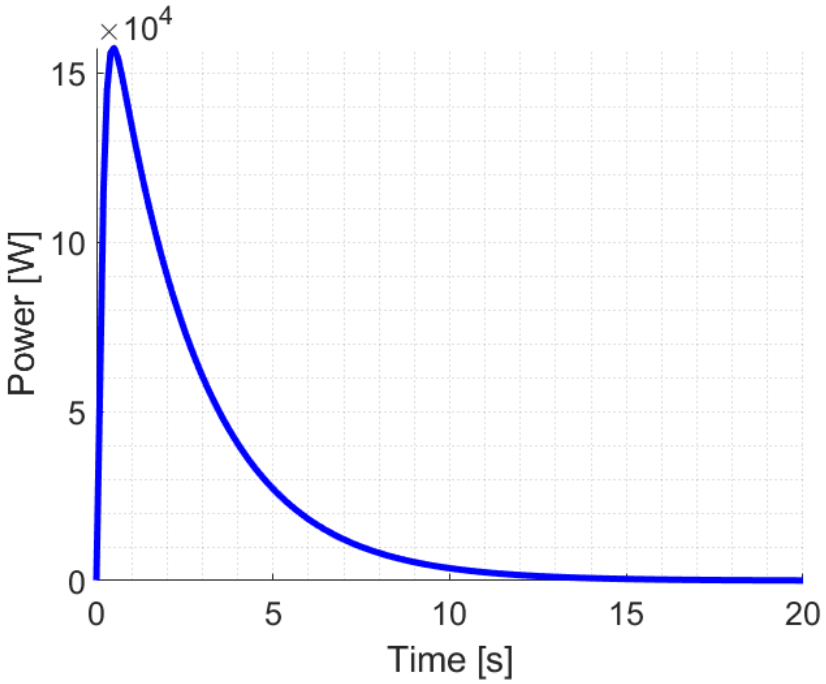


Figure 3.10: Integral power deposition in DTT TF coil structures. The origin of the time axes is imposed at the dump beginning.

As mentioned previously the tool is able to integrate the power, by means of boolean controls, not only on the entire structure volume, but also on part of it. This is the key point for a consistent coupling with the 4C code. Here below the example of average power density evaluated in sixteen subvolumes that are used for the 4C coupling (figure 3.11).

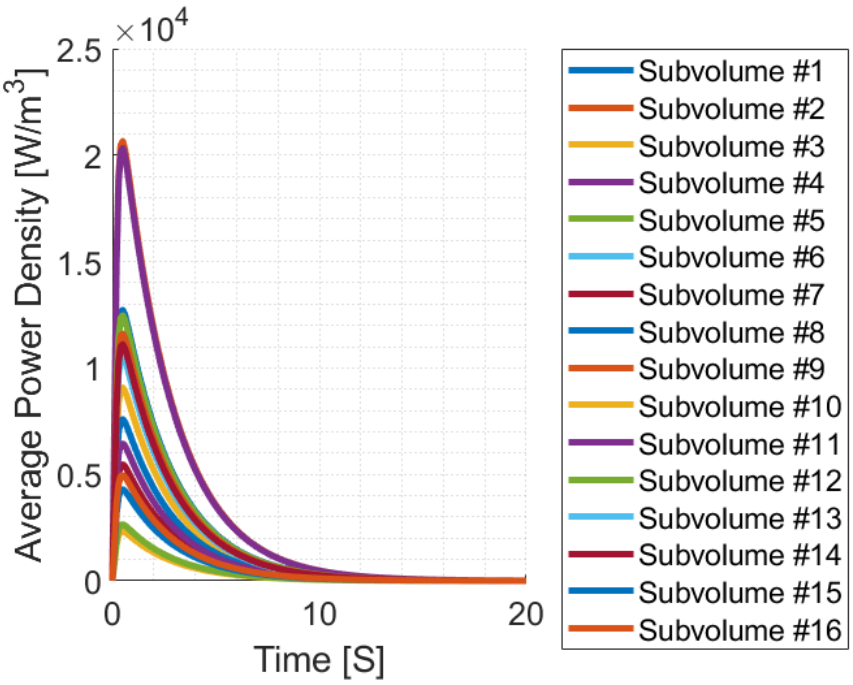


Figure 3.11: Average power density in sixteen subvolumes of the DTT TF coil structures.

This plot is proposed here only to show the potentialities of the tool, but the choice of the subvolumes and the procedure adopted for the average power density evaluation will be reported in the following chapter during the explanation of the coupling strategy with the 4C code.
As that the tool is fully 3D a detailed map of the power density can be obtained too as an outcome. In figure 3.12 the evolution of the power density in the equatorial section is shown.

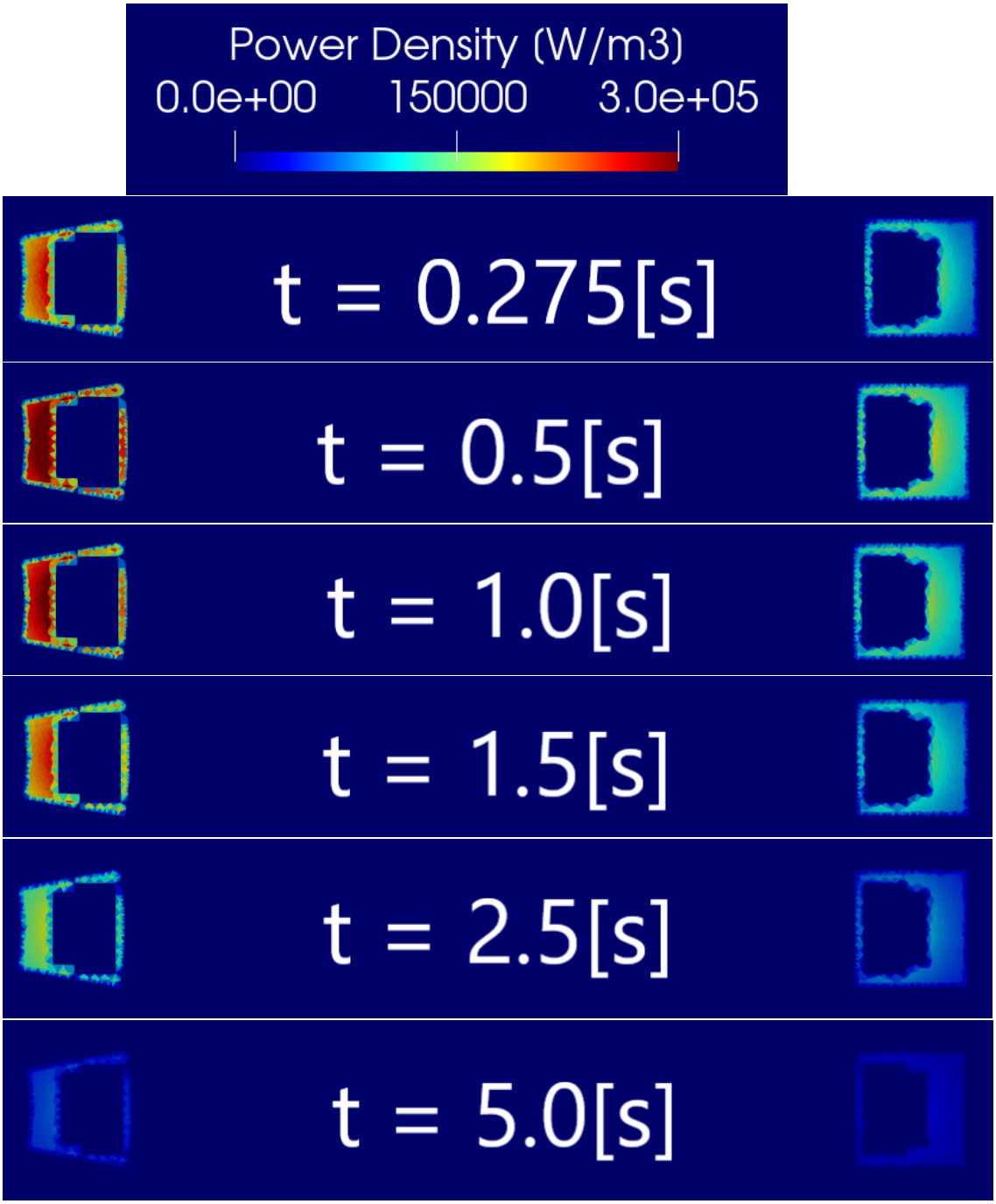


Figure 3.12: Evolution of the power density in the equatorial section. The time indicated must be intended measured from the dump beginning.

The initial steady state value is not shown given that no power deposition is expected. Looking at the evolution of the map in the six proposed instants it is possible to identify the evolution of the integral power value showing an initial increase followed by the expected decrease. Thanks to the map, it is possible to observe more in detail how the power is deposited, clearly seeing how the heat deposition is stronger at the inboard, where the geometry of the structure is more complicated offering big resistance to the current flowing. In the winding pack no power deposition is detected, as expected given that in the WP the only resistive part, the jacket, has been not modeled only considering the SC material uniforming the section as described in chapter 2.

Looking at both inboard and outboard section, the power deposition is not uniform on the section and shows the maximum value where more material is present, so in the outer side of the coil (with respect to the plasma). To predict a priori the spatial distribution of the power density was basically impossible, since two aspect should be considered: the fact that where the section is thinner the electric resistance is expected to be higher and the fact that where the resistance is higher the (induced) current is lower. Provided that the power deposition is proportional both to the resistance and to the current, it was not possible to be sure which of the two factor was actually predominant. By the way looking at the results obtained it seems that the dependence on the current is more relevant, coherently also to the fact that this dependence is actually on the second power of the current, while the dependence on the resistance is linear.

Given the non uniform distribution of the power density that is deposited in the structure the strategy of furthermore dividing the structure in smaller volumes, dividing the contribution of the plasma and non plasma side, will certainly improve the results and is considered to be a relevant possible future improvement of the tool.

# Chapter 4

# Thermal-hydraulic analysis: Coupling with the 4C code

The last main purpose of the work is to take the results of power deposition obtained from the electro-dynamic simulation and use them as an input for the thermal-hydraulic analysis aiming to evaluate the evolution of the temperature margin during the transient, given the presence of the power deposition due to eddy currents in the structures. In order to perform the thermal hydraulic simulations, the state of the art code 4C, developed at Politecnico di Torino, has been adopted.

## 4.1 Brief introduction on superconductivity phenomenology

The reasons for which the coupling between the electrodynamic model and the thermal - hydraulic one is required is hidden within the physics explaining the phenomenon of superconductivity.
Superconductive cables are excellent for the purposes of building magnets for fusion machines since they are capable of carrying huge currents with no resistance, but this status is not always present since it requires some specific conditions, combination of magnetic field, current density and temperature. Figure 4.1 shows in a qualitative way the constraint to be respected to obtain the superconductive state.

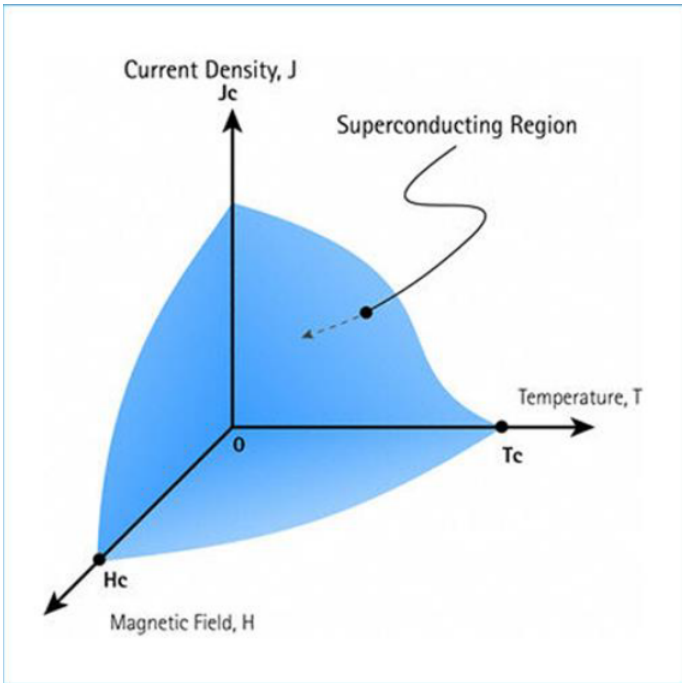


Figure 4.1: Qualitative representation of the superconductive region as a function of magnetic field, current density and temperature. Reproduced from [20].

As it is possible to understand from this plot, for each couple of values representing magnetic field and current density flowing in the strands, a single value of current sharing temperature exists, that is the threshold not to be overcome in order to avoid quench phenomena in the magnet.
During the transient that is analyzed in this work, the evolution of the current and of the magnetic field are known, but the variation of the latter causes AC losses in the strands and power deposition in the casing due to eddy currents, that are influencing the evolution of the strands temperature. For this reason it is relevant to monitor the evolution of the strands temperature and compare it locally with the current sharing temperature, function of both magnetic field and current density, in order to evaluate if quenching phenomena are foreseen during the transient.

## 4.2 Brief introduction to the 4C code

This section is mainly taken from [13].
The 4C (Cryogenic Circuit Conductor and Coil modeling) code is thought to perform simulations of the entire magnet system of fusion reactors mainly focusing on the winding (CICC), the structures and the refrigeration circuit with the final aim of predicting the coil performance in terms of temperature margin and heat load on the cryoplant. The code models simultaneously the cooling circuits for the winding and for the coil casing, coupling them respectively with the winding and the structures; the thermal coupling between the last two items is accounted too. The main model components that are present in the code are:

- 1D transient thermal-hydraulic model for the conductor and case cooling channel
- 2D heat conduction model of the structures (based on FreeFem++, the same adopted for the electro-dynamic model)
- 1D/0D compressible flow model for the cryogenic circuit (based on Modelica language and on ThermoPower and CryoModelica libraries)

The first model is based on the Multi - conductor Mithrandir code that is the evolution of the Mithrandir code, considering the simultaneous simulation of several conductors including the coupling between them. Detailed description of the code can be found at [14].
The second one is a simple heat conduction model developed with the open source finite element software FreeFem++ [5] that is directly and continuously interfaced with the model of the conductor and of the cooling channels. The solution of the 3D transient heat conduction problem in the bulky structures of the magnet is approximated by means of a series of 2D poloidal sections on which the problem is solved [15].
The last one is the representation of the cryogenic circuit by means of the object oriented language Modelica (Dymola interface [34]) that by means of 1D or 0D model reproduces the thermal - hydraulic behavior of the supercritial Helium that cools down the magnets.
The code has been validated against several experimental results [16], [17], on a wide range of transients and time-scales, and has been already used for predictive simulations [18], [19].

## 4.3 Coupling strategy between 4C code and the new developed electrodynamic tool

In order to complete the simulation of the selected transient, including the heat load coming from eddy currents, the coupling between the 4C code and the newly developed electrodynamic tool must be performed. As already mentioned previously, the tool is extremely flexible and it is possible to extract information correlated with the power deposition by eddy currents in a large variety of ways. To ensure the correct coupling, the tool has been implemented to produce as output the results that can be used as inputs by the 4C code.
The developed electrodynamic tool is fully 3D, but the 4C code does not solve the entire 3D thermal transient in the structures; on the contrary it simplifies the structures dividing it in segments that are represented by the central 2D cross section, and the heat load on that section is assumed to be equal to the average heat load on the segment itself. For this reason the electrodynamic tool produces as output the average power density evolution in different segments of the entire structures.
The first choice of the number segments to be adopted in the poloidal direction has been performed on the basis of the available 4C code model of the DTT TF coils. As the nuclear heat load has been provided to the 4C code as average power density in sixteen segments, shown in figure 4.2. So sixteen segments will be used as a first attempt for the analysis of the current fast discharge. The independence of the results from the number of 2D cross sections adopted will be assessed in the next future, as the analyses performed here are mainly demonstrative of a real application of the electrodynamic tool.
In order to obtain the average value of power density in each of the segments, the volume of the structures has been divided into the sixteen subvolumes thanks to some boolean controls and then, for each of them, the average power density has been evaluated as reported in equation 4.1, where the subscript $n$ stands for the n-th segment of the subdivision.

$$q_n^{III} = \frac{1}{V_n} \int_{V_n} \frac{1}{\sigma} \cdot \overrightarrow{J}^2_{eddy} dV_n \tag{4.1}$$

The electrodynamic tool produces as output a matrix in which the first column is the time and the remaining ones are including progressively the av-

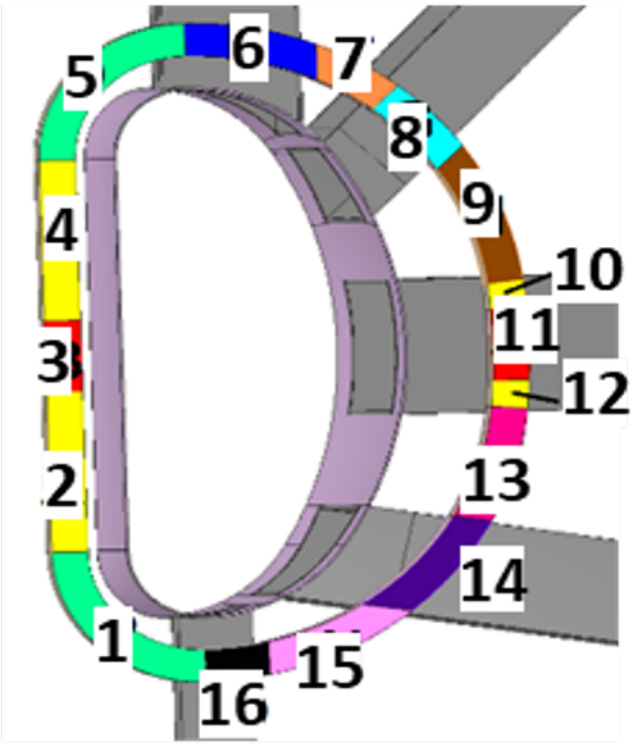


Figure 4.2: Subdivision of the structures of the DTT TF magnet for heat load definition.

erage power density in all the sixteen segments. To facilitate the reading procedure by the structure module of the 4C code, the matrix is disassembled and recomposed in as many files as the number of segments. Each of the files has two columns, the first one representing the time and the second the average power density in the correspondent segment.
The reading procedure of these files by the 4C code has been integrated in the already existing procedure simply adding a function able to import the files, read their content and then interpolate in time the values since the time discretization in the 4C code is adaptive and not necessary the same as that used to compute the power deposition in the structures by the electrodynamic tool. Once interpolated, the power density value is transmitted to the function generating the heat load to be passed to the FreeFem++ code solving the thermal transient in the structures. In such a way, with

a single simulation of the electrodynamic transient, is possible to perform as many thermal - hydraulic simulation as desired. Doing that the computational effort is reduced, loosing, however, the thermal feedback on the electro-dynamic simulation that could influence relevant material properties, i.e. the electrical conductivity of the structure steel. This issue may be faced in future as potential development of the tool.
The coupling strategy is summarized in a schematic way in figure 4.3 where the logic connection between the different models included in the tool are pointed out by red arrows.

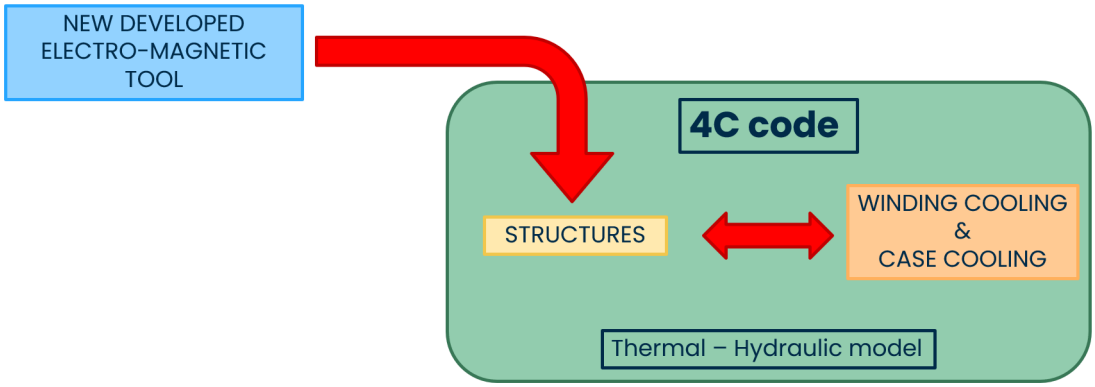


Figure 4.3: Schematic representation of the coupling strategy between the 4C code and the newly developed electro-magnetic tool.

The power density evolution evaluated in the sixteen segments in which the structures are subdivided has been already presented in the previous chapter with the aim of showing the capability of the tool in handling the results (figure 3.11).
This coupling strategy is functional but can be obviously improved. It could be possible to consider a non uniform heat load over the 2D section representing the segment aiming to better reproduce the real power distribution in the section as shown in figure 3.12, or even to increase the number of segments in which the overall coil is discretized along the poloidal direction. By the way, simply comparing the Joule power deposited in the structures evaluated directly by the tool with the approximation given by the 16 segments discretization, obtained multiplying the average segment power density

by the segment volume and summing them up, it is possible to observe that no big differences are actually detected as it is shown in figure 4.4.

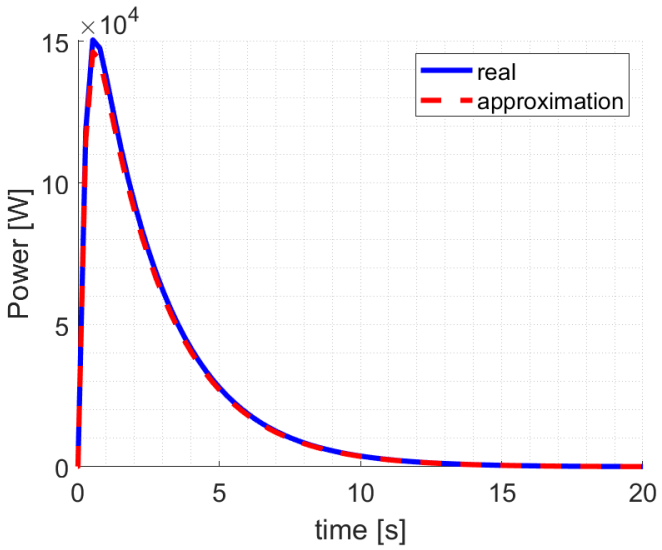


Figure 4.4: Comparison between Joule power computed by the 3D tool and its approximation obtained with the 4C segment discretization

The error obtained using the discretized version is evaluated on the base of the energy deposition during the transient. The deposited energy can be simply computed, by definition, as reported in equation 4.2.

$$E(t) = \int_{t_0}^{t} P(t)dt \tag{4.2}$$

The error is simply evaluated as percentage relative difference between the energy computed using the real power evolution (obtained directly with the 3D tool) and its discretized version (equation 4.3), obtaining a discrepancy of less than 3%. This discrepancy is considered to be acceptable, but however, as already mentioned, an improvement of the discretization can furthermore increase the precision of the approximation.

$$\epsilon_{rel} = \frac{|E_{corr} - E_{discr}|}{E_{corr}} \cdot 100 = 2.8\% \tag{4.3}$$

## 4.4 Simulation setup

The fast current discharge scenario is driven by the time evolution of the current carried by the coil. As already mentioned in chapter 3, the dump of the current is exponential with a time constant $\tau = 5.0[s]$. In the electrodynamic tool the current was ramped up to the steady state value that has been kept for few seconds and then the dump was performed, for numerical stability reasons. This current evolution is not useful in the thermal-hydraulic case and, thanks to the developed coupling strategy, it is possible to avoid including in the TH simulation non relevant part of the transient. Indeed in the 4C code only 10 [s] of nominal steady state before the dump have been modelled, to assure the stabilization of the values, and then the dump is induced as reported in figure 4.5.
The current flowing in the coil generates a magnetic field that is relevant for the evaluation of the current sharing temperature. The magnetic field, as already observed in the previous chapters, is not uniform on the section of the winding pack, and this means that is not uniform on the length of the pancake too. For completeness, the magnetic induction profile along three pancakes (P3, P5 and P10) is shown in figure 4.6.

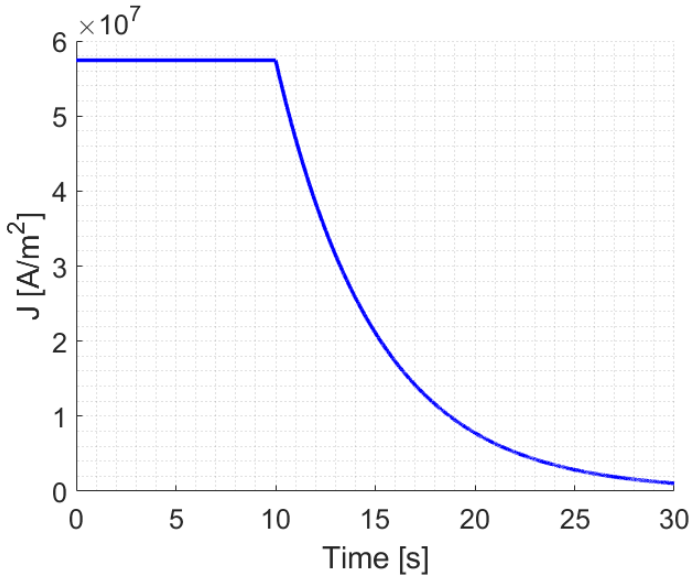


Figure 4.5: Module of the current density evolution in 4C simulation.

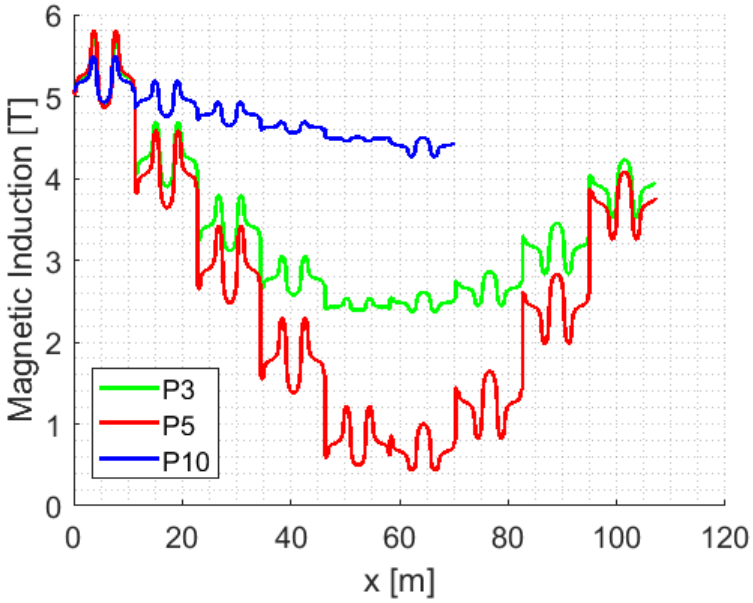


Figure 4.6: Magnetic induction profiles along pancakes 3, 5 and 10.

Moreover some static heat loads are always included in the analysis: the radiative heat load from the TS, cooled by helium at 80 [K] and the conductive heat load coming from the gravity support, quantified to be, conservatively, 30 W for each TF coil. The most relevant heat loads during the transient at hand, by the way, are those given partly by the AC losses and, mainly, by the deposited in the solids due to eddy current passing from the solid to the conductor. The nuclear heat load has been neglected here, as in the experimental campaign within the DTT cold test facility there will clearly be no plasma.
The 4C code is solving a fluid equation and proper boundary conditions are required. The 4C code allows to decide which kind of boundary condition to adopt. It is possible to fix them at pancakes and channels inlet and outlet (e.g. imposing the inlet temperature and the pressure at inlet and outlet, or the inlet temperature, one pressure and the mass flow rate), or, as alternative, connecting the model of the coil with the model of the feeding circuit. This circuit is fed by a circulator with a parabolic characteristic that is represented in figure 4.7, intersected with the circuit resistance.
Both the circuit and the circulator characteristics are obtained from nominal

data; then, the circulator characteristic has been properly scaled to the correct rpm ratio foreseen to be used in the real case application. The coefficient of the quadratic characteristic ($\Delta e = a \cdot Q^2 + b \cdot Q + c$) and the operative rmp ratio are reported in table 4.1.

Table 4.1: Pump characteristic data.

| **a** | **b** | **c** | $\omega/\omega_0$ |
|---|---|---|---|
| $-1.543 \cdot 10^7$ | $-1.899 \cdot 10^5$ | $1.589 \cdot 10^3$ | 1.575 |

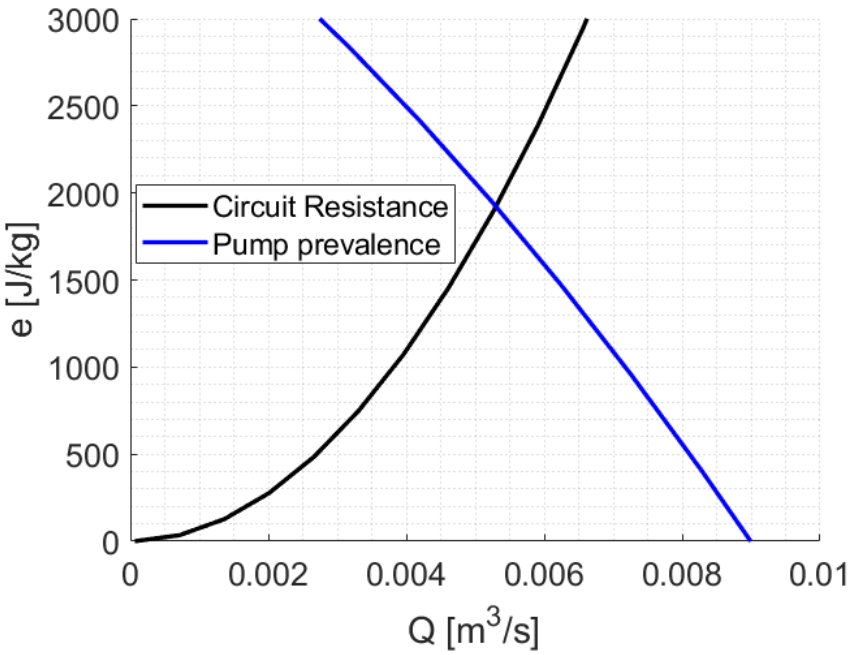


Figure 4.7: Pump characteristic and circuit resistance in the specific energy vs. volumetric flow rate plane, independent from the thermodynamic operating conditions.

The shown characteristic is that of the pump working in the operating conditions representative of the entire tokamak machine. For the case of

the stand alone simulation of one TF (as in the cold test facility) the flow rate obtained as outcome from the intersection between pump characteristic and circuit resistance is divided by the number of coil presents in the DTT tokamak configuration (18), given that they are eighteen parallel hydraulic circuits opposing the same resistance to the flow. From this assumption it is deduced that the flow rate is the same for each coil and so to obtain it, it is enough to divide the overall operated flow rate by the number of parallel coils.
The other components of the circuit are two heat exchangers that ensure the proper inlet conditions to the coils, one upstream the pump and one downstream it. Then there are three pipes: the return and the supply lines from and to the coils and the case cooling channel supply, see figure 4.8.
The geometrical data of the pipes are reported in Table 4.2.

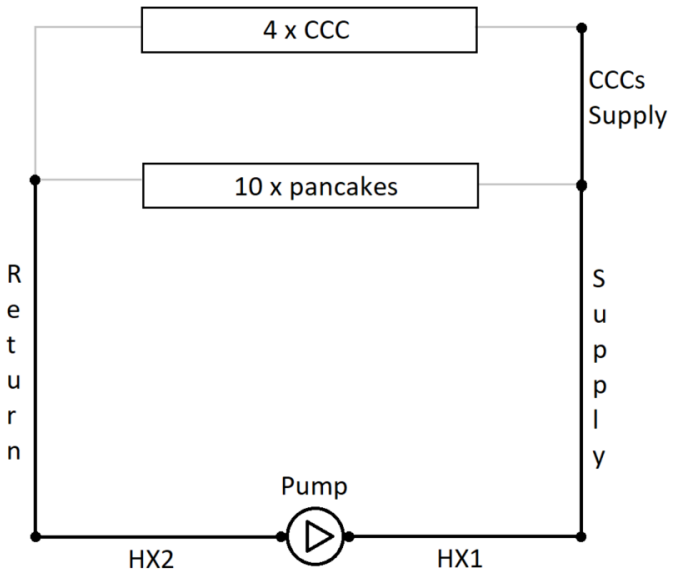


Figure 4.8: Qualitative representation of the circuit. Black lines = pipes.

Table 4.2: Geometrical data of the pipes of the circuit

| **Pipe** | **Length [m]** | **Diameter [m]** |
|---|---|---|
| HX1 | 30.0 | $2.0 \cdot 10^{-2}$ |
| Supply | 25.0 | $2.0 \cdot 10^{-2}$ |
| Return | 25.0 | $2.0 \cdot 10^{-2}$ |
| HX2 | 30.0 | $2.0 \cdot 10^{-2}$ |
| CCCs supply | 5.0 | $2.0 \cdot 10^{-2}$ |

At the inlet and outlet of each pipe, initial pressure and temperature values are imposed. What is relevant to mention is that both the supply of the pancakes and the supply of the case cooling channels are at the same initial condition of pressure ($p = 5[bar]$) and temperature ($T = 4.55[K]$), and all the hydraulic channels (pancakes and case cooling channel) are connected to the same return manifold at an initial pressure of $3[bar]$. To avoid having discrepancies between the amount of flow in the short and long pancakes, due to the different hydraulic resistance, the throttling valves (that will exist in the real machine for the homogenization of the mass flow rate in different hydraulic channels having different length) are introduced. The initial return manifold temperature has been set at $4.9[K]$, that is an estimation of the temperature at the outlet of the coils subjected only to the static loads. Moreover the initial temperature distribution along the pancakes is a linear increasing profile from the inlet value of $4.55[k]$ to the outlet value of $4.90[K]$.

## 4.5 Thermal - hydraulic simulation results.

The first relevant result coming out from this simulation is the amount of power that, coming from the structures, reaches the winding pack. This result is relevant since not all the power that is deposited in the structures reaches the winding pack, thanks to the direct cooling of the casing by means of the casing cooling channels, but its however the direct responsible of the strands temperature increase. This is a first of a kind computation for the DTT TF analyses, since the 4C code model of those coil has never been used before with an eddy current load generated directly in the structures.
The power generation is that already plotted in figure 4.4, while the power that is transmitted to the winding pack is shown in figure 4.9.

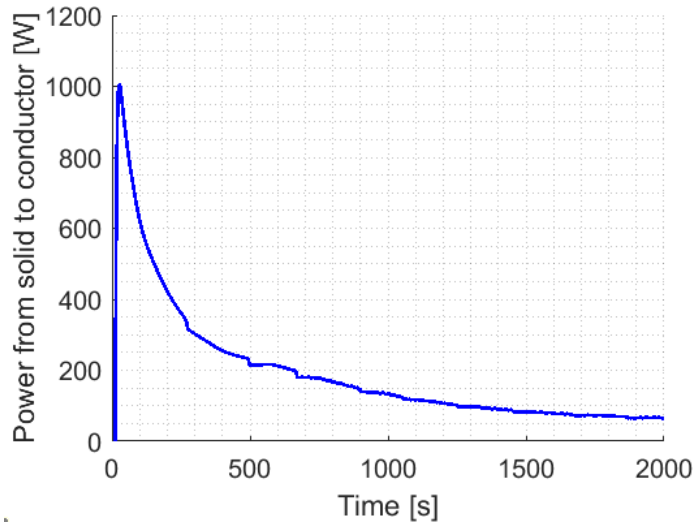


Figure 4.9: Power transferred across the ground insulation from the solid structures to the winding pack.

Simply looking at this plot, and comparing it to the power generation one, it is easy to observe the different time scales of the two evolution. The power generation is extremely fast and within few current decay time constants ($\tau = 5[s]$) the heat load goes basically to zero; on the contrary, the power that is passing to the winding pack shows a qualitative evolution that is similar to the one of the power generation, but on time scales that are longer: indeed after $2000[s]$ the power that is passing to the WP is still of the order of $100[W]$. This is due to the processes of heat transfer across the insulation layers and within the bulky structures, that are influenced by their thermal capacity, thermal conductivity and density, influencing the thermal diffusivity and thus the heat transfer time constant.
This power is that actually influence the thermal behavior of the winding pack, impacting on the supercritical helium and strands temperature.
The presence of a power deposition in the superconductive strands causes an increase of their temperature. This phenomenon must be carefully monitored for the reasons reported in section 4.1 with main reference to figure

4.1. Indeed a temperature increase may translate into an overcoming of the current sharing temperature that may cause a quench in the magnet.
During the analyzed transient, all the variables are changing; by the way, the only way in which the superconductive state can be lost is due to a temperature increase, since the strands are designed to assure superconductivity while carrying the nominal current and sustaining the nominal magnetic field. During this transient these values are only going to decrease, starting from nominal conditions, and so only the overcoming of the critical temperature may be responsible of the loss of superconductive state. For this reason the temperature is the variable to be controlled. The current sharing temperature is a function of both current and magnetic field, and it is directly evaluated during the transient by the 4C code.
The first location in which temperature modifications are induced is clearly within the structures, where the power generated by eddy currents is deposited. As representative of the thermal transient within the structures, the evolution of maximum and minimum temperature in the two equatorial sections is shown in figure 4.10. Moreover, the temperature map on the same section 10 seconds and 90 seconds after the start of the current dump are shown in figure 4.11 and in figure 4.12. In this particular case, the equatorial inboard section is also representative of the maximum temperature within the structures that is located in the vertical leg.

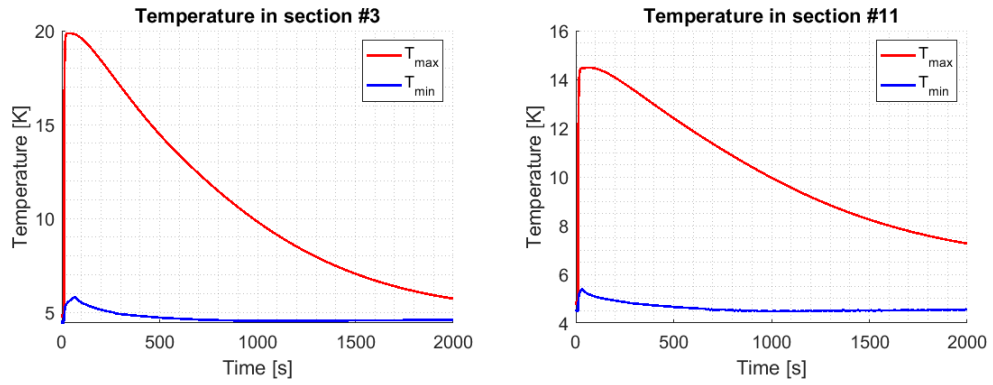


(a) (b)

Figure 4.10: Maximum and minimum temperature evolution in the two equatorial sections. Section 3 = inboard (a), section 11 = outboard (b).

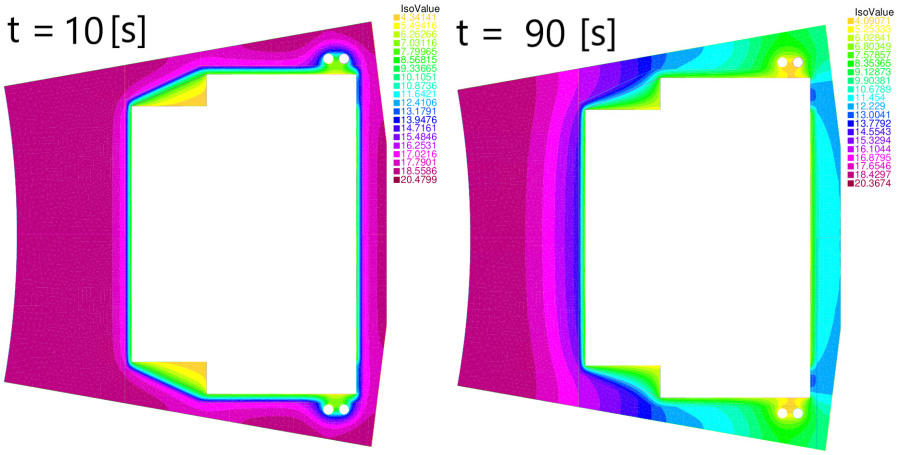


Figure 4.11: Temperature map at the inboard equatorial section. The time indicated must be intended measured from the dump beginning.

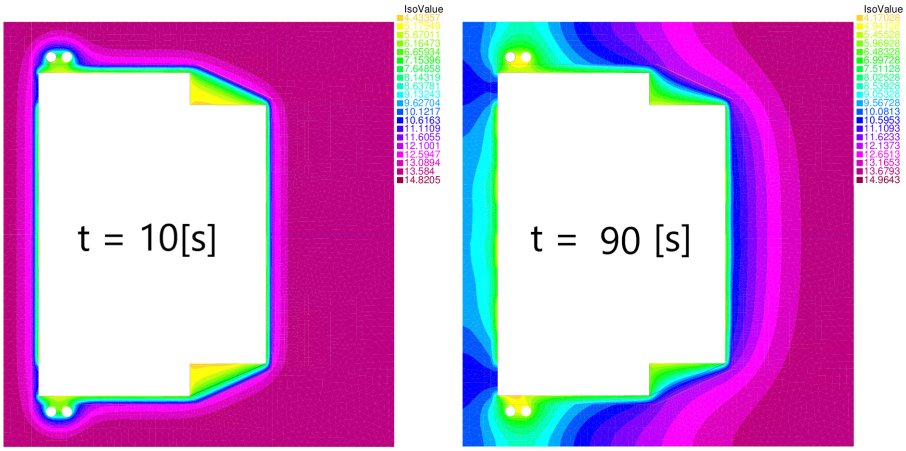


Figure 4.12: Temperature map at the outboard equatorial section. The time indicated must be intended measured from the dump beginning.

Looking at the plot of the temperature evolution it is possible to observe how the two sections behave in different ways, both for what concerns the magnitude of the peak and for what concerns its width. The higher temperature reached in the inboard section is due to the higher heat load that exists in correspondence of that segment, as it is possible to see from the

comparison plot in figure 4.13.

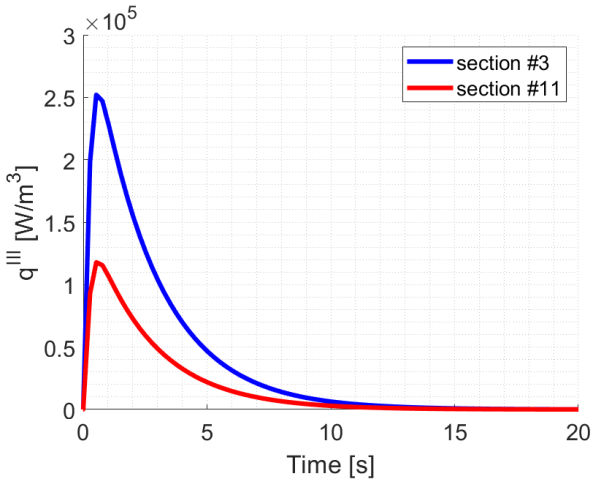


Figure 4.13: Heat load on the inboard and outboard equatorial sections. Section 3 = inboard, section 11 = outboard. The time indicated must be intended measured from the dump beginning.

By the way the time scale of the power deposition in the two sections is the same, and so it can not be the responsible of the different speed of the recooling. This difference in speed may be due to the higher mass of the outboard section and consequently its higher thermal inertia with respect to the inboard one.
Looking at the temperature maps, it is also possible to verify that the cooling of the structures is stronger close to the cold winding pack and to the four cooling channel present in the casing, as expected.
As reported before, a fraction of the power that is generated in the structures reaches the winding pack, causing its temperature increase. Also in this case, the temperature increase is not uniform, and it has been studied by means of 1D models for each pancake included in the winding pack. Each pancake has its own behavior and so all of them must be considered in the analysis. Also within the same pancake the temperature has a distribution that is not uniform, but what is relevant to be controlled is the hot spot temperature, that is the point within the pancake with the highest temperature, the most critical condition with respect to the risk of overcoming the current sharing temperature. The hot spot evolution, for each pancake is plotted in figure

4.14.

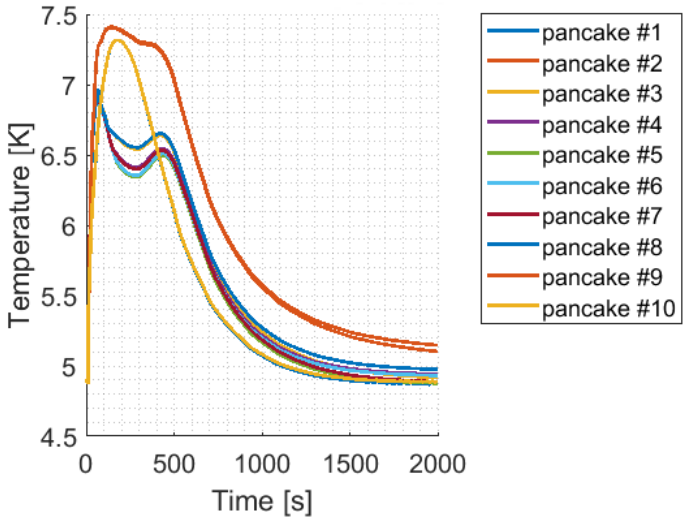


Figure 4.14: Evolution of the hot spot temperature in the ten pancakes.

The first observation is that a symmetric behavior, with respect to the WP toroidal symmetry axes, is detected, with the two shorter and lateral pancakes (number 1 and 10) that show an evolution qualitatively different from the remaining eight pancakes with a single peak, the second and ninth pancakes that are the hottest and the central pancakes that behaves in a very similar way to each other. The symmetric behavior is coherent with the symmetric nature of the geometry that is also producing a symmetric magnetic field.
It is relevant to understand the reasons behind this different behavior of some pancakes and the reason of the existence of two peaks in the hot spot evolution of the central pancakes. The presence of two peaks seems to be counter intuitive given that there are no drivers that show this kind of evolution. In order to understand the reason of this behavior, the temperature evolution recorded in some specific points along the pancake has been analyzed, with the aim of including in the analysis the transport phenomena that are due to the supercritical helium flow.
The sensors have been fixed all along the length of the pancake every 5 meters. For explanatory reasons, only two representative pancakes have been

selected and compared: the number 5, that is one of the two pancakes exactly at the center of the winding pack, and the number 10, that is one of the external pancakes, which clearly present differences for what concerns the hot spot temperature evolution. In these two cases, the temperature evolution is shown in four sensors along the pancake at 5, 35, 70 and 100 meters for the fifth pancake and at 5, 25, 50 and 70 meters for the tenth one (which is shorter), and can be seen in figure 4.15 and figure 4.16.

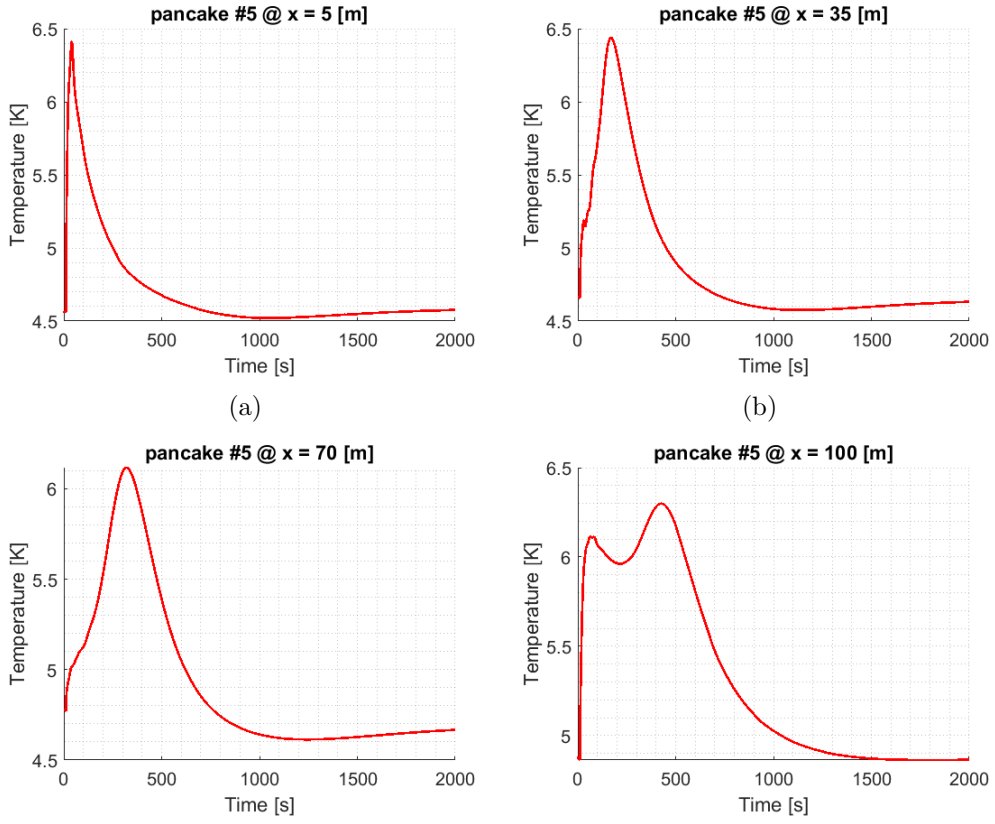


Figure 4.15: Temperature evolution at the selected sensors in pancake 5. Evolution at 5 [m] (a), 35 [m] (b), 70 [m] (c) and 100 [m] (d).

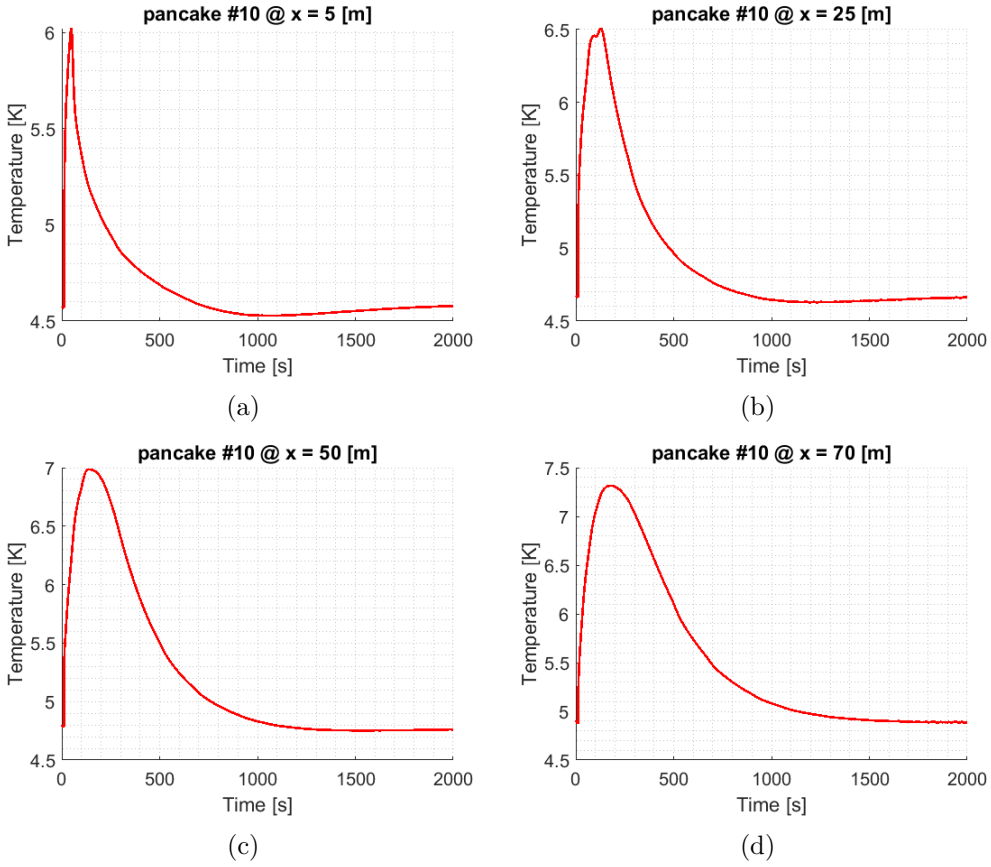


Figure 4.16: Temperature evolution at the selected sensors in pancake 10. Evolution at 5 [m] (a), 25 [m] (b), 50 [m] (c) and 70 [m] (d).

Looking at the plotted evolutions, it is possible to recognize the behavior already observed in the hot spot temperature evolution with the formation of the two peaks moving towards the outlet of the pancake in the central channels, while in the lateral pancake only a single peak is present. These plots are consistent with the double peak behavior of the hot spot temperature in lateral pancakes, but they are not explaining the reason of that. In order to understand it, the distribution of the power deposition along the pancake must be observed (figure 4.17).

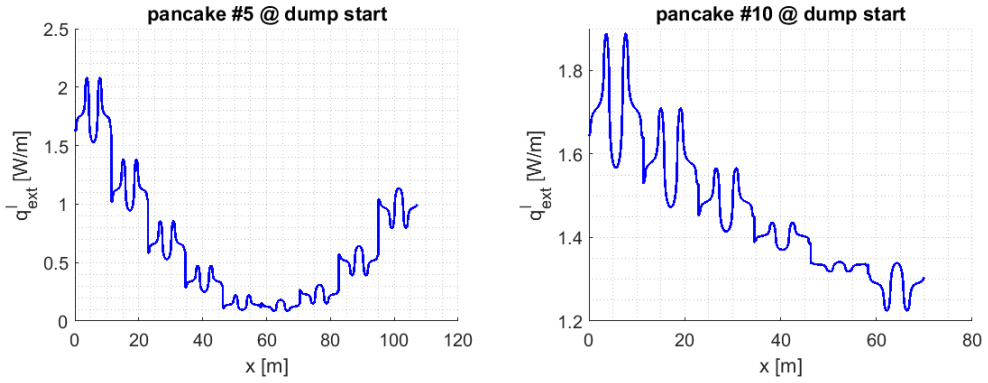


(a) (b)

Figure 4.17: Power distribution along the pancakes 5 (a) and 10 (b).

In pancake 10, the power deposition is decreasing moving towards the outlet of the pancake. In such a way, the peak is generated basically immediately at the inlet and then is transported towards the outlet by the helium flow. On the contrary, in pancake 5 the power is deposited mainly at the inlet and at the outlet of the pancake. This causes the generation, at the beginning of the power deposition, of two hot spots, one at the inlet, the other at the outlet. Looking at the temperature evolution in the last sensor (close to the outlet) two peaks are detected since the first is the one generated by the power deposition in that point, the second is the one generated at the inlet and then transported at the outlet by the helium flow. This thesis is also confirmed by the distance in time between the two peaks. Looking at the helium flow velocity evolution, taken as an example from pancake 5, (figure 4.18) it is possible to assume that, on average, the flow moves at a speed of 0.24 [m/s]. At this velocity, the distance between the inlet of the pancake and the sensor located at 100 [m] is covered in almost 420 [s]. This time is called the transit time and is absolutely comparable to the time distance between the two peaks.

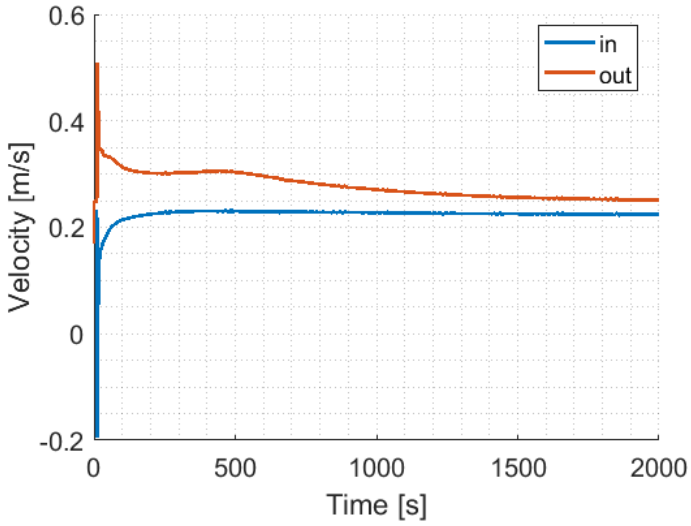


Figure 4.18: Helium flow velocity at inlet and outlet of pancake 5.

Knowing the hot spot temperature evolution is then possible to focus on the temperature margin, that is evaluated, in the case of $Nb_3Sn$ strands, considering the current sharing temperature evaluated at the equivalent magnetic field. The latter is the uniform magnetic field that results in a critical current equal to the integral of the critical current density across the cable cross section when the (real) magnetic field, varying on the cable cross section, is known.
The current sharing temperature, depending on other conditions (namely the magnetic field and the current density) is not uniform along the pancake over the transient. This means that it is not possible to fix a value of critical temperature and actually compare it with the hot spot temperature, but the temperature margin must be evaluated in each point, and the attention will be paid at the position where the minimum temperature margin is reached. In figure 4.19 the evolution of the minimum temperature margin is plotted.

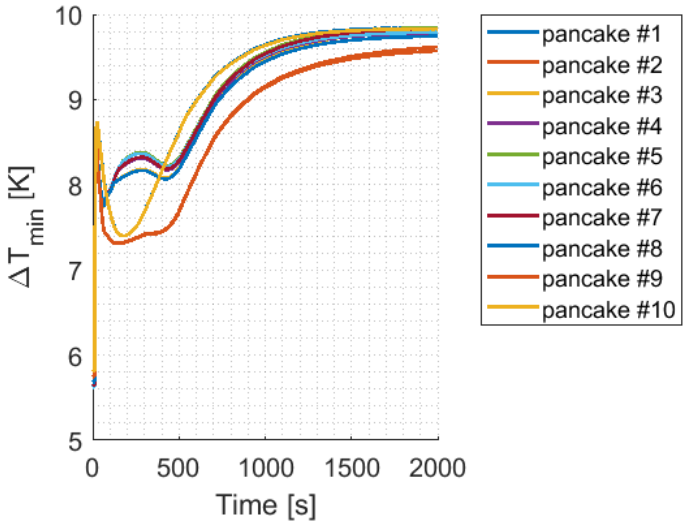


Figure 4.19: Minimum temperature margin during the transient

The immediate consequence of this plot is that during the selected transient the magnet is never overcoming the current sharing temperature and this means that no quench is expected to happen during the fast current discharge of DTT TF coil during the cold test in the cold test facility. This is due to the fact that, how it is possible to understand from figure 4.1, decreasing the magnetic field and decreasing the current density flowing in the conductor, the current sharing temperature increases, naturally avoiding to have current sharing phenomena in the cable. To better understand the phenomena, the plot of the evolution of the minimum of the current sharing temperature is proposed too (figure 4.20). It is important to remember that this is not necessary the value against which the minimum temperature margin is evaluated, by the way it is helpful to understand how generally the current sharing temperature evolve. The evolution is coherent with what has been pointed out previously. Indeed the current sharing temperature is increasing monotonically from its steady state value (different for each pancake since each of them is subjected to different magnetic field) to the asintotic value given that current and magnetic field are both approaching to zero, point at which the maximum current sharing temperature, for the selected material, is detected.
This phenomena helps avoiding the excessive erosion of the temperature margin, but, however, the hottest temperature reached in the strands during the

transient, is never overcoming the minimum value of current sharing temperature, reason for which no quench is initiated.

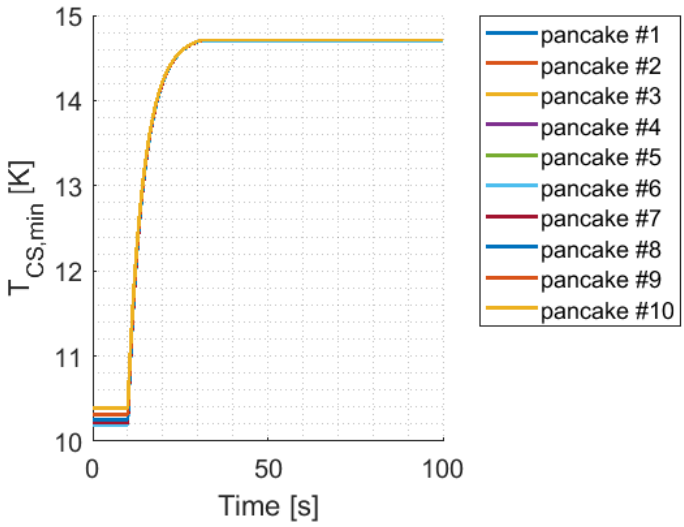


Figure 4.20: Evolution of the minimum current sharing temperature, in the cold test facility operating conditions.

In the proposed simulation, the coil structure is considered to be not in thermal contact with the winding pack on the plasma side since this is what happens normally during plasma burns due to the strong Lorentz forces that arise during the operation. By the way this assumption is not fully conservative in the case of a fast discharge given that the decrease of the current and of the magnetic field during th transient causes also the decrease of the Lorentz forces. This causes a re-attachment of the coil structure with the winding pack.By the way this process of re-attachment is not known in detail and it is not even known if once at zero current and zero magnetic field the structure is back in full contact with the winding pack, due to some possible (partial) plastic deformations.
In order to be fully conservative, a second run of the simulation has been performed considering full contact between the coil structure and the winding pack also on the plasma side. The comparison between the minimum temperature margin within the hottest pancake (number 2)in the two extreme cases (full contact and no contact) is shown in figure 4.21.

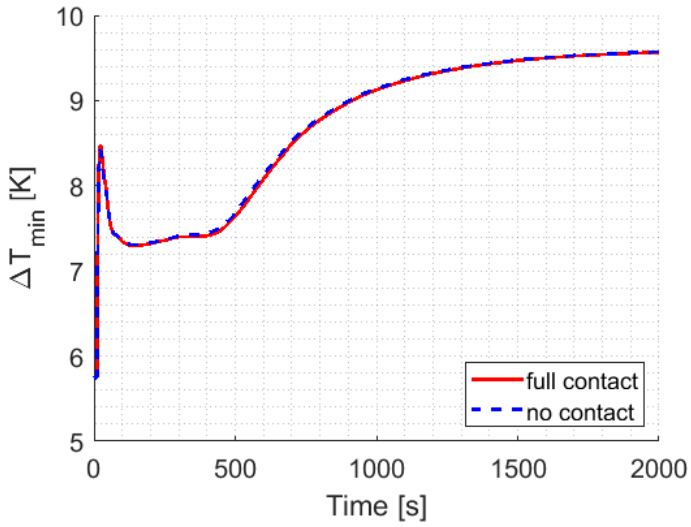


Figure 4.21: Comparison between the evolution of the minimum temperature margin in case of full contact and no contact between coil structures and winding pack on the plasma-facing side.

From this figure it is possible to observe that the thermal contact on plasma side is a minor effect on the temperature evolution within the winding pack, given that the difference between the extreme cases, no contact and full contact, is negligible. This means that not knowing how actually the re-attachment between structures and winding pack occurs during the transient is not a main issue for the transient at hand.

The results discussed in this section demonstrate that no quenches are expected during a fast current discharge in a single TF of DTT in conditions relevant for thei cold test, also in the first seconds (which are considered the most critical, since the magnetic field and the current density are still high and the current sharing temperature is, for this reason, low).

# Chapter 5

# Conclusions and perspectives

The magnetic confinement of the plasma in fusion reactors is a strongly multi-physical problem and an important technological and scientific challenge. A lot of different aspects must be considered during the design and operation phases; in this framework, the numerical simulations provide a significant contribution, helping both with the design and the future operation of the magnets.
This thesis aims at proposing a first of a kind electro-magnetic tool capable to be coupled with the already existent and validated tool for the thermal - hydraulic simulation of superconducting magnets for fusion reactors: the 4C code. The aim was to include in the simulation of the transients also the contribution given by the power deposition generated by the eddy currents within the coil structures in presence of a time varying magnetic field, caused either by normal pulsed tokamak operation or by off normal transients (e.g fast current discharge or disruption). The time varying magnetic field generates, according to Faraday law, an electric field that induces, in conductive materials as the structures, currents that, by Joule effect, generate a non negligible power deposition close to the winding pack, influencing the temperature margin of the superconducting cables.
The idea proposed in this work is the development of the above mentioned tool with an open source code (FreeFem++) to be as much flexible as possible both in the stand alone use of the tool but, especially, in the coupled use with the 4C code
A first magnetostatic analysis has been performed solving the weak formulation of the steady state Ampère law with the A - formulation, using the magnetic vector potential as unknown of the problem. The tool has been

verified against a simple analytical case (the Biot-Savart law [30]), and then against reference data obtained with the commercial code OPERA [28]at ENEA of the static magnetic field generated by the DTT TF coil both in stand alone and tokamak configuration [31]. The milestone obtained with this first step is that an open source code has been able to reproduce precisely the results obtained by state of the art software for magnetostatic analysis.
After that, the development of the transient tool has been described, introducing the time dependent part of the Ampère law and properly translating it in the A - formulation version, founding out the connection between the magnetic vector potential, unknown of the problem, and the generated electric field, fundamental for the evaluation of the eddy currents.
The developed tool has then been successfully benchmarked against results from some classical literature benchmark and state of the art finite element software (Comsol [29]).
The tool has then finally been applied to a real case: the fast current discharge in one single DTT TF coil. The obtained results show, as expected, an integral power deposition that in the very first instants after the dump shows a peak and then follows the driver behavior decreasing exponentially its value. The power deposition is not uniform all over the coil, but the 3D nature of the tool allows to consider also this heterogeneity for the coupling with the 4C thermal - hydraulic model.
The complete EM+TH simulation of the fast current discharge in one single DTT TF coil has been performed and presented. The major outcomes are the evolution of the temperature margin, the evolution of the hot spot temperature and the power that from the structure is passing to the winding pack. As a consequence of these results it is possible to conclude that during a fast current discharge in the DTT TF coil in the cold test facility no quench is expected to happen, even if a non negligible temperature increase is foreseen, due to the increase of the current sharing temperature due to the simultaneous decrease of the magnetic field and current density flowing in the coil.
This work can be seen as the beginning of the development of more detailed and complete tools for SC magnets system simulations, and many future possible development can be implemented, related to several different topics. Improving the structure discretization, and developing a continuous and direct coupling between the two tools such that temperature dependent properties can be correctly evaluated at each time step could be a first future tool

improvement. The impact of the modification of physical properties (mainly electrical conductivity) due to temperature evolution is not known yet, but to evaluate it, before the possible development of the continuous and direct coupling, some sensitivity analysis can be performed.
A subsequent step will certainly be the validation of the tool against experimental data, soon available thanks to the cold test facility experimental campaign foreseen for the next couple of years.
Finally the introduction of other physical models is envisaged. A relevant add on may be the thermal - mechanical model of the structure, relevant to evaluate the effect of fast transient on the magnet integrity or to optimize the (slow) cool down strategies.

# Acknowledgement

A warm thank you must be dedicated to all the people that helped me to complete this thesis work, both from the practical, technical and scientific point of view and from the emotional one.
A special mention to my supervisors Roberto Bonifetto and Andrea Zappatore that always made me feel comfortable during my work. A great thank you for their availability too, even in the "smart working" mode that we were obliged to adopt due to COVID-19 pandemics.
A warm thank you also to professor Pierre Jolivet for his precious support provided in the FreeFem++ forum.
I can not obviously forget to thank my family and my girlfriend that from the first day supported me and my work. And finally a special mentioning to all my friends and the wonderful people that I had the chance to met in the last years that made the university experience unique not only from the cultural point of view, but also from the human one.
I want to thank figuratively the thesis experience too. I have the full awareness of having learned a huge amount of things, hard to be founded in books. And the best has yet to come...

# Bibliography


[1] F. Romanelli. *Fusion Electricity. A roadmap to the realisation of fusion energy.* EFDA - November 2012

[2] ENEA. *DTT. Divertor Tokamak Test facicily. Interim Design Report*

[3] Alfio Quarteroni, Fausto Saleri, Paola Gervasio. *Scientific Computing with MATLAB and Octave*. Fourth Edition. Springer

[4] Hang Si. *TetGen. A Quality Tetrahedral Mesh Generator and 3D Delaunay Triangulator. - Version 1.6 - User's Manual*, 2020

[5] Frèdèric Hecht. *New development in FreeFem++.* Journal of numerical mathematics, 2012, vol. 20, no 3-4, p.251-266

[6] Gabriele D'amico, Alfredo Portone and Cornelis T.J. Jong. *An Electromagnetic and Structural Finite Element Model of the ITER Toroidal Field Coils.* IEEE Transactions on applied superconductivity, Vol. 28, No. 3, 2018.

[7] Oszkar Birò, Kurt Preis, Christian Paul. *The use of a reduced vector potential $A_r$ formulation for the calculation of iron induced field errors.* IGTE, Graz, Austria.

[8] Oszkar Birò. *Edge element formulations of eddy current problems.* Computer methods in applied mechanics and engineering, Vol. 169, pp. 391-405, 1999.

[9] Akihisa Kameari. *Results for benchmark calculations of problem 4 (the felix brick).* COMPEL - The international journal for computation and mathematics in electrical and electronic engineering. Vol. 7 pp. 65-80.

[10] MUltifrontal Massively Parallel Solver (MUMPS 5.4.0) Users' Guide. April 13, 2021

[11] Gmsh Reference Manual. The documentation for Gmsh 4.8.1. Afinite element mesh generator with built-in pre- and post-processing facilities. 22 March 2021

[12] L.Ridgway Scott, Terry Clark,Babak Bagheri. *Scientific Parallel Computing*. Princeton Univerity Press. 2005

[13] L. Savoldi Richard, F. Casella, B. Fiori and R. Zanino. *The 4Ccode for the cryogenic circuit conductor and coil modeling in ITER*. Cryogenics, 50, 2010, pp. 167-176.

[14] L. Savoldi and R. Zanino. *M&M: Multi-Conductor Mithrandir Code for the Simulation of Thermal-Hydraulic Transients in Super-Conducting Magnets*. Cryogenics, 40, 2000, pp. 179-189.

[15] *4C CODE (version 2)(Cryogenic Circuit Conductor and Coil) USER'S MANUAL*. Dipartimento di Energetica, Politecnico di Torino, Italy. Report # PT DE 609/IN. November 2010.

[16] R. Zanino, R. Bonifetto, R. Heller and L. Savoldi Richard. *Validation of the 4C Thermal-Hydraulic Code against 25 kA Safety Discharge in the ITER Toroidal Field Model Coil (TFMC)*. IEEE Transactions on Applied Superconductivity, 21(3), pp. 1948-1952, 2011.

[17] R. Bonifetto, A. Kholia, B. Renard, K. Rißе, L. Savoldi Richard, and R. Zanino. *Modeling of W7-X superconducting coil cool-down using the 4C code*. Fusion Engineering and Design, 86(6), pp. 1549-1552, 2011.

[18] R. Zanino, D. Bessette, L. Savoldi Richard. *Quench analysis of an ITER TF coil*. Fusion Engineering and Design, 85, pp. 752-760, 2010.

[19] R. Bonifetto, P. K. Domalapally, G. M. Polli, L. S. Richard, S. Turtu', R. Villari, and R. Zanino. *Computation of JT-60SA TF coil temperature margin*. Fusion Engineering and Design, 86(6), pp. 1493-1496, 2011.

[20] Prof. Francesco Laviano. *Lectures of the seminar on superconductivity for the course "Advanced Materials for Nuclear Applications"*. A.Y. 2019-2020.

[21] *Handbook on Materials for S.C. Machinery.* NBS Boulder (yellow book). 1977

[22] A. Di Zenobio. *DTT TF coils description (DTT TF coils_R=219_V7_rev02.pdf).* https://www.dtt-dms.enea.it/share/page/dtt-document-version-page?nodeId=4b8d8132-21bb-469f-b0c8-e2bb5278e9cf&site=dtt&version=2.1

[23] A.Anemona. *DTT TF coil CAD model (02_01_TFC_02092020_DTT2020_03013.zip).* https://www.dtt-dms.enea.it/share/page/dtt-document-version-page?nodeId=bc93fc41-7f4d-4f44-bd55-0b5e8010c567&site=dtt&version=2.0

[24] Prof. Pierre Jolivet. *Expert Tutorial: Parallel tools.* FreeFem days 2020

[25] R. Albanese and G. Rubinacci. *Finite Element Methods for the Solution of 3D Eddy Current Problems.* Advances in imaging and electron physics. Vol. 102 1998

[26] C. S. Biddlecombe, E. a. Heighway, J. Simkin and C. W. Trowbridge. *Methods for Eddy Curret Computation in Three Dimensions.* IEEE transactions on magnetics, Vol. MAG-18, No. 2. March 1982

[27] EUROfusion. *European Research Roadmap to the Realisation of Fusion Energy*

[28] *OPERA-3D REFERENCE MANUAL.* February 2004

[29] COMSOL. *Introduction to COMSOL Multiphysics 5.6.* 2020

[30] P. Mazzoldi, M. Nigro, C. Voci. *Elementi di Fisica. Elettromagnetismo e Onde - Seconda edizione.* EdiSES s.r.l. 2008

[31] S. Tortù, February 1, 2021, personal communication.

[32] OpenCASCADE technology - online documentation. Available at https://old.opencascade.com/doc/occt-7.5.0/overview/html/index.html (last seen October 2, 2021).

[33] FreeCAD - online documentation. Available at https://wiki.freecadweb.org/Main_Page (last seen October, 3 2021).

[34] *Dymola (Dynamic Modeling Laboratory) User's Manual, Version 5.3.* DYNASIM AB, Lund, Sweden. 2004